

Physical and dynamical properties of the main belt triple asteroid (87) Sylvia

Jérôme Berthier, Frédéric Vachier, Franck Marchis, Josef Durech, Benoit Carry

▶ **To cite this version:**

Jérôme Berthier, Frédéric Vachier, Franck Marchis, Josef Durech, Benoit Carry. Physical and dynamical properties of the main belt triple asteroid (87) Sylvia. Icarus, 2014, 239, pp.118-130. 10.1016/j.icarus.2014.05.046 . hal-01018599

HAL Id: hal-01018599
https://hal.science/hal-01018599

Submitted on 4 Jul 2014

HAL is a multi-disciplinary open access archive for the deposit and dissemination of scientific research documents, whether they are published or not. The documents may come from teaching and research institutions in France or abroad, or from public or private research centers.

L'archive ouverte pluridisciplinaire **HAL**, est destinée au dépôt et à la diffusion de documents scientifiques de niveau recherche, publiés ou non, émanant des établissements d'enseignement et de recherche français ou étrangers, des laboratoires publics ou privés.

Physical and dynamical properties of the main belt triple asteroid (87) Sylvia[☆]

J. Berthier[a,*], F. Vachier[a], F. Marchis[b,a], J. Ďurech[c], B. Carry[a]

[a] *Observatoire de Paris, CNRS UMR8028, Sorbonne Universités, UPMC Univ Paris 06, IMCCE, 77 avenue Denfert Rochereau, 75014 Paris, France*
[b] *Carl Sagan Center, SETI Institute, 189 Bernardo Avenue, Mountain View CA 94043, USA*
[c] *Astronomical Institute, Faculty of Mathematics and Physics, Charles University in Prague, V Holešovičkách 2, 18000 Prague, Czech Republic*

Abstract

We present the analysis of high angular resolution observations of the triple asteroid (87) Sylvia collected with three 8–10 m class telescopes (Keck, VLT, Gemini North) and the Hubble Space Telescope. The moons' mutual orbits were derived individually using a purely Keplerian model. We computed the position of Romulus, the outer moon of the system, at the epoch of a recent stellar occultation which was successfully observed at less than 15 km from our predicted position, within the uncertainty of our model. The occultation data revealed that the moon, with a surface-area equivalent diameter $D_S = 23.1 \pm 0.7$ km, is strongly elongated (axes ratio of 2.7 ± 0.3), significantly more than single asteroids of similar size in the main-belt. We concluded that its shape is probably affected by the tides from the primary. A new shape model of the primary was calculated combining adaptive-optics observations with this occultation and 40 archived light-curves recorded since 1978. The difference between the $J_2 = 0.024\,^{+0.016}_{-0.009}$ derived from the 3-D shape model assuming an homogeneous distribution of mass for the volume equivalent diameter $D_V =$

[☆] Based on observations collected at the European Southern Observatory, Paranal, Chile (089.C-0944, 087.C-0014, 385.C-0089, 085.C-0480, 077.C-0422, 074.C-0052), at the Gemini North Observatory in Hawaii, and at the W. M. Keck Observatory. The Keck observatory was made possible by the generous financial support of the W. M. Keck Foundation.

[*] Corresponding author
Email address: berthier@imcce.fr (J. Berthier)

273 ± 10 km primary and the null J_2 implied by the keplerian orbits suggests a non-homogeneous mass distribution in the asteroid's interior.

Keywords: Asteroids, Satellites of asteroids, Adaptive optics, Photometry, Orbit determination, Occultations

1. Introduction

The minor planet (87) Sylvia is a main belt asteroid discovered in 1866 by Pogson (1866). In the 1990s, frequency analysis of photometric observations hinted that this asteroid could be binary (Prokof'eva and Demchik 1992, 1994; Prokof'eva et al. 1995). Its first satellite (S/2001 (87) 1, known as *Romulus*) was discovered in February 2001 by Brown et al. (2001) using the Keck II telescope atop Hawaii's Mauna Kea. Three years later, Marchis et al. (2005b) announced the discovery of a second companion (S/2004 (87) 1, known as *Remus*), using the European Southern Observatory's Very Large Telescope (VLT). Sylvia became the first known triple asteroidal system. Since then, eight others have been discovered and studied (Brown et al. 2005; Bouchez et al. 2006; Ragozzine and Brown 2009; Brozović et al. 2011; Descamps et al. 2011; Fang et al. 2011; Marchis et al. 2010, 2013b).

Asteroid (87) Sylvia is the largest member of a collisional family born, at least, several hundreds of million years ago, more probably between 1 and 3.8 Gyr. The age of this family, for which more than 80 members have been identified among current census of asteroids, is commensurable with the evolutionary timescales of Sylvia's satellite system (Vokrouhlický et al. 2010). Various authors estimate that the system is dynamically very stable over a large timescale (at least one million years, see Winter et al. (2009); Vokrouhlický et al. (2010); Fang et al. (2012)), the satellites being in a deeply stable zone, surrounded by both fast and secular chaotic regions due to mean-motion and evection resonances (Frouard and Compère 2012).

Observations led to the determination of the dynamical and physical properties of the system. Asteroid (87) Sylvia is classified as a X-type asteroid

(Bus and Binzel 2002) located in the outer main belt ($a \simeq 3.49$ AU, $e \simeq 0.09$, $i \simeq 11°$), within the large Cybele-zone, with a volume-equivalent diameter estimated to 278 ± 11 km, a relatively low density of 1.31 ± 0.15, and a large macro-porosity estimated to $52 \pm 11\%$ (Carry 2012, and references therein). The two moons, Remus and Romulus, with a diameter respectively estimated to ∼7 km and ∼18 km (from photometry measurements, Marchis et al. 2005a) or 9–12 km and 5–16 km (derived by Fang et al. 2012, as a free parameter of their dynamical model), orbit at a distance of ∼700 km and ∼1350 km from the primary. Finally, Fang et al. (2012) estimates dynamically that Sylvia is oblate with a J_2 value in the range 0.0985–0.1.

We report here on new results on the dynamical and physical properties of Sylvia's system based on the analysis of adaptive-optics imaging, light-curves and stellar occultation data (Section 2). We improve Sylvia's 3-D shape model and estimate its overall size (Section 3.1). We estimate the shape and size of the outer satellite Romulus from the analysis of the latest observed stellar occultation (Section 3.2). We improve the determination of orbital parameters for the two satellites, we estimate the mass and density of Sylvia, and we examine its quadrupole term J_2 (Section 4). Finally, we discuss the surprising elongated shape of Romulus revealed by this stellar occultation.

2. Observations and data

2.1. Adaptive-optics observations

We gathered in the VOBAD database (Marchis et al. 2006a) all observations, acquired by our group or already published, from February 2001 to December 2012 recorded in the near-infrared with adaptive-optics (AO) systems available on large ground-based telescopes. We use the ESO Very Large Telescope NACO imaging camera (Lenzen et al. 2003; Rousset et al. 2003) and SINFONI spectro-imaging camera (Eisenhauer et al. 2003), the Gemini North ALTAIR AO system (Herriot et al. 2000) with its camera NIRI (Hodapp et al. 2003), and the NIRC2 camera on the Keck II telescope (Wizinowich et al. 2000; van Dam et al. 2004).

The AO frames were recorded in broad band filters (J, H, or K, from 1 to 2.5 μm) and were all processed in a similar manner. The basic data processing (sky subtraction, bad-pixel removal, and flat-field correction) applied on all these raw data was performed using the recommended eclipse data reduction package (Devillard 1997). Successive frames taken over a time span of less than 6 min, were combined into one single average image after applying an accurate shift-and-add process through the Jitter pipeline offered in the same package. Data processing with this software on such high signal-to-noise ratio data (>1000) is relatively straightforward. Since these data respect the Shannon's theorem, it is possible to retrieve completely the continuous signal from the knowledge of enough samples. After re-sampling each image to 1/10th of the pixel level, the centroid position on each frame can be accurately measured by a Gaussian fit. The final image is obtained by stacking the set of frames with individual shifts determined from cross-correlation. Once processed, individual images reveal the resolved shape of the primary (angular size $\sim 0.2''$), and, sometimes, the unresolved image of the satellites appears. We used a dedicated algorithm (Hanuš et al. 2013a) to extract the contour of the primary and to determine its photocenter, from which we measured the astrometric positions of the satellites by fitting a Moffat-Gauss source profile.

Figure 1 displays Sylvia's system as seen by VLT/NACO and Keck/NIRC2 instruments after the processing has been applied. Table 1 provides the observing condition at each epoch of image acquisition. Tables 2 and 3 summarize all the astrometric measurements used to fit the orbits of the two satellites of Sylvia. The accuracy on the observing time is the result of the computed mean time of the jittered images, typically 0.2s to 1s depending on the observatory where the data were recorded.

2.2. Hubble space telescope data

Storrs et al. (2001) reported the confirmation of the presence of Romulus on Hubble Space Telescope (HST) images collected on February 23, 2001 with the WFPC2 instrument through various filters. We retrieved from the HST

archive the three unsaturated observations taken through the F439 filter with an individual exposure time of 3s. These observations were re-processed using our own pipeline reproducing the HST/WFPC2 cookbook method. The resulting image, shown in Fig. 1, confirmed the detection of Romulus at a position very close to the one reported by Storrs et al. (2001). The second satellite, Remus, is also visible and detected closer to the primary at a distance of 0.34″. The positions of the satellite were derived using the same Moffat-Gauss profile fit than for our AO observations. Interestingly, even though Marchis et al. (2005a) reported the triple nature of (87) Sylvia from observations taken in August 2004 and onward, this February 2001 HST observation was in fact the first detection of the third component of the system. We included these astrometric positions for Romulus and Remus in our analysis, which is particularly useful for Remus since it increases the observational time span by 1264 days (∼931 revolutions).

2.3. Light-curve data

We used 40 light-curves observed from 1978 to 1989 published by Harris and Young (1980), Schober and Surdej (1979), Weidenschilling et al. (1987), Weidenschilling et al. (1990), Blanco et al. (1989), and Prokof'eva and Demchik (1992). The data were compiled by Lagerkvist et al. (1987) in the Uppsala Asteroid Photometric Catalog, now available through Internet (APC[1] Web site). To this set of dense light-curves we added sparse photometry from US Naval Observatory (IAU code 689), Roque de los Muchachos Observatory, La Palma (950), and Catalina Sky Survey Observatory (703). See the works by Ďurech et al. (2005) and Hanuš et al. (2013b) for details on sparse photometry.

2.4. Stellar occultation data

The observation of a stellar occultation consists in recording the time of immersion and emersion of the star in front of which the asteroid passes, as seen by geographically distributed observers along the occultation path. Each

[1] http://asteroid.astro.helsinki.fi/apc

observed occultation point is then projected onto a common plane that passes through the center of the Earth, and lies perpendicular to the direction of the star as seen from the occulting body. Assuming that the relative velocity of the body with respect to the observer is well estimated by the ephemeris, which is a soft assumption, especially for numbered asteroids, one can transform the timings into lengths, and then evaluate the size of the occulting body. We get several segments - the chords - which are directly proportional to the size of the cross-section of the body as seen by observers. With a sufficient number of chords, the silhouette of the body is drawn, and can yield a strong constraint on its 2-D profile in the occultation plane.

The observation of a stellar occultation by an asteroid is one of the few methods which can yield the size and the overall shape of the asteroid without hypothesis on its physical nature. If several independent events of the same occulting body are collected then a 3-D model of the asteroid can even be determined (Drummond and Cocke 1989). However, due to the low number of well-covered events for a given asteroid, full 3-D reconstruction based on stellar occultations only will always concern a small sample of asteroids. Stellar occultations have however proved to be useful to scale the convex shape models of asteroids derived by light-curve inversion (Ďurech et al. 2011).

Four stellar occultations by Sylvia have been reported in the past 30 years, but only a total of four chords (three for an event, one for another, none for the two others) have been collected (Dunham et al. 2012). These occultation data are therefore useless to scale Sylvia's shape model (Kaasalainen et al. 2002). The stellar occultation by Sylvia successfully observed in early 2013 is thus the first opportunity to do so.

On January 6, 2013, about 50 European observers were mobilized to observe the occultation of the TYCHO-2 1856-00745-1 star by (87) Sylvia (Berthier et al. 2013). Among them, 19 observers have recorded a negative event (i.e., no disappearance of the star), and 13 observers have reported a successful observation of the event, providing 16 chords including 4 of the occultation by Romulus. The bad weather forecast on western Europe this night prevented other ob-

servers to record the event. Figure 2 shows the result of the observation of this stellar occultation. Table 4 presents the timings of the event recorded by observers (published on Euraster[2] Web site), and table 5 lists the observers and the geodetic coordinates of the observing sites.

Stellar occultations by asteroids are usually observed by a group of observers who use different acquisition and timing devices. As a consequence, the accuracy on the measurements differs from one observer to another, and sometimes measurements can disagree owing to systematics in the calibration of the absolute timing reference. A typical example is a chord which is clearly shifted with respect to other chords nearby. The latter can then be used to estimate the offset to apply on the chord to restore its timings. However, it can be tricky to shift the timings of chords, mainly because no evident rule can be found. In such cases it is better to decrease the weight of uncertain chords with respect to accurate ones.

For the January 6, 2013 stellar occultation by Sylvia, we are confident in the absolute timings of the chords as most timing references were insured by GPS or atomic clock time servers (see Tab. 5). We considered only two chords as discrepant (see column "Offset" of Tab. 4). The first shows a clear lateness of a few seconds with respect to the three chords immediately next to it (one north, two south). The offset we apply (-3.8s) sets the chord back in alignment with the three others. The second discrepant chord shows a slight lead on a nearby chord for which the observer can assert the time of the disappearance. The offset we apply (+0.5s) shift the chord forward in alignment with the latter. As we empirically changed the timings of these two chords, we down-weighted their timings to one thousandth of the weight affected to other chords.

At the mean time of the occultation, January 6, 2013 01:37:06.46 UTC, the computed geocentric orbital velocity of Sylvia is 17.1 km/s. With timing uncertainties lying in the range 0.03–1 s (with a mean value of 0.25 ± 0.3 s), we can expect to measure lengths with a mean accuracy of 4 km ($\sim$1.5% of Sylvia's

[2] http://euraster.net/results/2013/

size), which corresponds to ∼2 mas at the geocentric distance of Sylvia.

3. Shape and size of the system components

3.1. Shape and size of Sylvia

A convex shape model of Sylvia was previously derived by Kaasalainen et al. (2002). They used 32 light-curves observed in 8 apparitions spanned over 1978 - 1989, which allowed them to derive a unique model with ECJ2000 pole direction (71°, +66°). As was later shown by Marchis et al. (2006b), this model agreed well with AO observations. It also agrees with the occultation data presented here.

To further improve the fit and to include all data types into the modeling, we used the KOALA algorithm (Carry et al. 2010, 2012). It can simultaneously fit optical light-curves, occultation data and image profiles to give a best-fit 3-D shape model represented by a non-convex polyhedron (Kaasalainen 2011). Contrary to standard light-curve inversion, where light-curves are fitted by a convex shape model, the best-fit solution is harder to define in case of multiple data sources. Different types of data have to be weighted to compose the total χ^2 as a measure of the goodness of fit (Kaasalainen 2011). Moreover, given the low number of 2-D profiles available, the non-convex shape solution had to be regularized to suppress unrealistic small-scale fluctuations of the shape. The shape was approximated by a polyhedron described by a spherical harmonics series of the order and degree five or six. This resolution was sufficient to model details of the occultation profile, and still low enough to suppress artificial details that often appeared with higher resolution.

The KOALA algorithm minimizes the total $\chi^2 = \chi^2_{\rm LC} + w_{\rm AO}\chi^2_{\rm AO} + w_{\rm Occ}\chi^2_{\rm Occ}$ that composes the individual contributions from light-curves (LC), adaptive optics profiles (AO), and occultation chords (Occ). Adaptive optics and occultation data are weighted with respect to the light-curves with parameters $w_{\rm AO}$ and $w_{\rm Occ}$, respectively. The optimum values of these weights (so called maximum compatibility weights) can be obtained following the approach of Kaasalainen

(2011). In our case, the shape of the $\mathcal{S}$ surface was 'shallow', thus the optimum weights were not well defined – an order of magnitude range of $w_{\rm AO}$ and $w_{\rm Occ}$ was possible. We varied weights of AO and occultation data with respect to light-curves to see how the models evolved, then we selected only solutions that gave acceptable fits to the data. Thus, instead of one best solution, we obtained a set of slightly different models that all fit the data well, each with a slightly different spin, shape, and size. One of these models is shown in Fig. 3, and the fits to the light-curves, image and occultation profiles are shown in Fig. 4. The discrepancy between one AO image contour and the model silhouette comes from an over-estimation of the AO contour due to poor seeing conditions at the time of this observations. The root mean square (RMS) residual of the occultation fit is 2.6 km, which is below the accuracy provided by the timings (see 2.4).

To further estimate the uncertainty of our model, we created many clones of the original data set and processed them the same way as the original data. For light-curves, we re-sampled the set with random sampling and replacement – so each new clone consisted of the same light-curves, but some were missing and some were included more times. This approach is similar to the bootstrap method (Press et al. 2007), the difference is that we re-sampled the whole light-curves, not individual measurements, because points within one light-curve cannot be treated as fully independent measurements. By this approach, we can roughly sample the range of possible solutions. For occultation data, we randomly changed the timings using a normal distribution law, with reported uncertainties as standard deviations. Because of the low weight of the AO data in the process, we left them unchanged. The distribution of shapes and spin axis directions then represented the variance of the model given the data and served for a realistic estimation of the model uncertainties. The width of 3σ error intervals reported in Table 6 corresponds to the maximum spread of the relevant parameters across our sample of bootstrap models obtained with different $w_{\rm AO}$ and $w_{\rm Occ}$ weights.

Figure 5 displays the RMS residuals between synthetic and observed light-

curves as function of the spin-vector coordinates (grid interval of 2°on the ECJ2000 celestial sphere). For one of the formally best solutions (based on the total χ^2), the direction of the spin axis (70°, +69°) is almost the same as for the convex model of Kaasalainen et al. (2002), and the 3-D shapes are similar overall. The standard deviation of the pole direction is about 3° in ecliptic longitude and 1° in ecliptic latitude. The volume-equivalent diameter for the best model is D_V= 273 km, and J_2 = 0.024. The basic physical parameters are listed in Table 6. We also used different resolutions of the model (the degree and order of spherical harmonic expansion used for the shape parametrization) and different weightings between the data to assert the stability of the solution. The plausible shape models cover a range of equivalent diameters from 266 to 280 km and J_2 spans the range 0.015 – 0.040.

Using our 3-D shape model, we estimated for each image the offset between the center of mass and the photocenter, assuming an uniform density distribution. They span the intervals [-2.3, +1.9] mas in x, and [-0.4, +1.8] mas in y, and are, at least, five time smaller than the uncertainties of the astrometric measurements (see Tables 2 and 3). We have not taken into account these offsets in the astrometric measurements used to fit orbits.

3.2. Shape and size of Romulus

The analysis of the chords of Romulus give us the opportunity to determine its size and, for the first time, to estimate its shape. The distribution of the 4 observed chords is not sufficient to model without ambiguity the profile of the satellite, but they are sufficiently well distributed to estimate its size and biaxial dimensions. The parameters of the ellipsoidal profile (coordinates of the center x_0, y_0, axis radii a, b, and position angle from North of the major axis ψ) are calculated from the set of conics which best fit the n points of coordinates $(x_i, y_i)_n$, which correspond to the coordinates of the extremity of the chords as measured by the observers. We solve the system of linear equations by the linear least-squares method of the Singular Value Decomposition method (Press et al. 2007). Each fitted points is assigned initially a standard deviation calculated as

the quadratic mean of the observational uncertainties.

Even if our system is overdetermined ($n = 8$ equations for 5 parameters), the solution can be singular, or numerically very close to singular. In that case, we reduce the system to 3 parameters by fixing the coordinates of the conic center (x_0, y_0). Then we define a grid of values with a given step size, and we solve the equations for each point of the grid, searching for the conics which have $\Delta\chi^2 < 14.2$, the 3–σ confidence region for the normal distribution with 3 degrees of freedom (Press et al. 2007).

Among the observers, two could have observed the occultation by Romulus, namely M. Bretton and V. Fristot (c.f. Tab. 4 and 5). The first one made a naked eye observation and stop too early to observe Romulus event. The analysis of the video acquired by the second confirms that no occultation of Romulus occurred along his path. This result sets a strong upper limit on the size of Romulus, which allows us to reject all the fitted conics which intersect this chord.

Considering a range of 20 km wide for the coordinates of the conic center, and a grid step size of 10^{-3} km, the best-fit conic profile of Romulus is (Fig. 6):

$$\begin{aligned} a &= 19.0\,\text{km} \quad \pm 1.6\,\text{km} \\ b &= 7.0\,\text{km} \quad \pm 0.4\,\text{km} \\ \psi &= 112.4\,^\circ \quad \pm 13.2\,^\circ \end{aligned}$$

with uncertainties at 3–σ. It implies a mean axis ratio $a/b = 2.7 \pm 0.3$, and a surface-area equivalent diameter $D_S = 23.1 \pm 0.7$ km.

This result relies on the reliability of the timings of the two northern chords of Romulus. Even if P. Tanga failed to report accurate absolute timings, he was able to estimate them using the computer clock (synchronized by NTP) used to control the camera, and to measure precisely the duration of events and the delay between the two events (see Tab. 4). Using the 3-D shape model of Sylvia projected into the occultation plane, we can tie the time of the first disappearance of the star observed by P. Tanga to other timings with an accuracy smaller than 0.2s. In the case we shift Tanga's chords by +0.2s, the

axis ratio of the best-fit profile of Romulus decreases to 2.2, with $a = 18$ km, $b = 8$ km, $D_S = 24$ km, and equivalent uncertainties.

4. Dynamical overview on Sylvia system

Orbital solutions for Sylvia's satellites have been recently published by Fang et al. (2012), and previously by Marchis et al. (2005a) at the occasion of the discovery of the second satellite. We take the opportunity of the successful observation of a stellar occultation by Romulus to test the reliability of its orbital solution, used to predict the event (Berthier et al. 2013), and to improve the orbital parameters of the two satellites.

4.1. Reliability of Romulus orbit

We used our genetic-based algorithm *Genoid-Kepler* (Vachier et al. 2012) to predict the position of Sylvia's satellites for the January 6, 2013 stellar occultation. The dynamics used to model the orbit of the satellites was a pure 2-body Keplerian problem (no mutual perturbation between the two satellites was applied). For Remus, we used 25 astrometric positions (acquired in 2001, 2004, 2010 and 2011) spanning 3948.7 days or 2910.6 revolutions. For Romulus, we used 65 astrometric positions (acquired in 2001, 2004, 2005, 2006, 2010 and 2011) spanning 3953.8 days or 1317.9 revolutions. Tables 1, 2 and 3 detail the observing condition and the astrometric positions used for this work. The best solutions obtained give orbits with a RMS of 12.1 mas for Remus, and 11.2 mas for Romulus.

The successful observation of the occultation by Romulus highlights the reliability of our dynamical model. Figure 6 shows the goodness of the prediction of Romulus position with respect to Sylvia's center of mass (as defined by the 3-D model). The offset between the observed position of Romulus (e.g., defined by the center of the fitted profile) and its predicted position is $\Delta x = -3.3$ km, $\Delta y = -13.1$ km (x and y are positive toward East and North). This predicted position is located at 13.5 km from the observed position. In the occultation

plane, the distance between the fitted profiles of Sylvia and Romulus is 1154.6 km. The geocentric orbital velocity of Sylvia being 17.1 km/s, the occultation by Romulus occurred 67.6 s later than Sylvia event. At this epoch, January 6, 2013 01:38:14.02 UTC, we infer the astrometric position of Romulus relatively to Sylvia's center of mass: $(x, y) = (590, -113) \pm 1.5$ mas.

4.2. New orbital solutions

We added this astrometric position into *Genoid-Kepler* input dataset, as well as an astrometric position acquired in 2010 with VLT/SINFONI (Marchis et al. 2013a). It increases the time span of data from 3953.8 to 4338.7 days or 1446.2 revolutions. This does not change significantly the dynamical solution of Romulus (RMS = 11.2 mas). Table 7 presents the orbital parameters of Sylvia's satellites obtained with *Genoid-Kepler*, and figure 7 displays the residuals (the difference between the observed O and computed C positions of the satellite and the primary) normalized by the positional uncertainty σ. The orbital solutions indicate that the satellites follow a quasi circular orbit, nearly coplanar (very low mutual inclination, lesser than 0°.5), and nearly aligned with the primary equatorial plane (by ∼4°). The average residuals are $dx = -0.4 \pm 11.9$ mas, $dy = 4.7 \pm 11.5$ mas for Remus, and $dx = 0.5 \pm 12.7$ mas, $dy = 0.6 \pm 9.4$ mas for Romulus (uncertainties at 3-σ), matching the level of accuracy of the observations. At the epoch of the occultation, the reliability of the model can be estimated by the difference between the observed and computed positions of Romulus, which are $dx = 0.2$ mas and $dy = -8.9$ mas, or $\Delta x = 1.0$ km and $\Delta y = -13.3$ km in the occultation plane. We inserted these orbital solutions in the Web service Miriade[3] of our Virtual Observatory Solar system portal, allowing everyone to compute the ephemeris of Sylvia's satellites.

The mass of Sylvia can be derived from the best-fit keplerian orbit of the satellites (see Tab. 7). Assuming the Gaussian gravitational constant and the solar mass, one can easily derive, independently, the mass of Sylvia from the

[3] http://vo.imcce.fr/webservices/miriade/

semi-major axis and the orbital period of each satellite (neglecting its own mass). We find $M_S = 1.380 \pm 0.151\ 10^{19}$ kg from Remus, and $M_S = 1.476 \pm 0.128\ 10^{19}$ kg from Romulus, considering the 1–σ uncertainties of the parameters. It is interesting to note that the two masses are consistent within their uncertainties. The mass derived from Romulus orbit is also very similar, by ∼0.5%, to that found by Fang et al. (2012), although it has been obtained by the latter by the fit of a fully dynamical three-body model.

From the mass of Sylvia and its volume, defined by its 3-D shape model, we infer its density. We find 1.29 and 1.38 g.cm^{-3} from Remus and Romulus data respectively, with an uncertainty of ± 0.16 g.cm^{-3}, taking into account the 1–σ uncertainties of the parameters. The resulting density of 1.34 ± 0.21 g.cm^{-3} is slightly lower, although consistent, with the average density of X-type asteroids of 1.85 ± 0.81 g.cm^{-3} (Carry 2012). The composition and meteorite analogs of X-types is still debated, and proposed analogs encompass CV and CO carbonaceous chondrites, enstatite chondrites, aubrites, mesosiderites, and even iron, stony-iron meteorites (Barucci et al. 2005; Vernazza et al. 2009, 2011; Ockert-Bell et al. 2010; Fornasier et al. 2011), which density ranges from 2.8 to 7.7 g.cm^{-3}. Although we do not have information on the composition of Sylvia, its density, lower than that of its most-likely components, indicates the presence of voids and/or pockets of very low density material (e.g., ices). The macroporosity we derive here ranges from 52% to 82% depending on the density of the analog meteorite.

4.3. Examination of the quadrupole term J_2

We used our *Genoid-ANIS* algorithm (Vachier et al. 2012) to search for a possible influence of an irregular mass distribution, considering the amount of voids determined above. We initialized the problem with $J_2 = 0.024$, the value estimated from the 3-D shape model (see Sec. 3.1). We search for orbital solutions in the space $0 \leq J_2 \leq 0.2$, all other parameters being free. The results are shown in Fig. 8. Assuming that the directions of the orbital poles of the satellites must be nearly aligned with the primary pole of rotation (hypothesis

justified by the low inclination of orbital planes, see Sec. 4.2), we discard all solutions for which coordinates of orbital poles are outside the 3–σ confidence interval of the primary spin-vector coordinates (see Sec. 3.1 and Fig. 5). We find that the best candidate solutions are obtained for $J_2 \to 0$. It means that no significant precession effect of the apsidal and nodal nodes is detected, and that the purely Keplerian orbit is enough to fit the available data to their accuracy.

Winter et al. (2009) showed that Sylvia's system is not stable unless the primary has a minimal amount of oblateness, at least 0.1% of the assumed primary J_2 of 0.17 reported by Marchis et al. (2005a). This oblateness provides a faster stabilizing effect on the satellites' orbits than other gravitational perturbations (e.g., Sun, Jupiter, see also Frouard and Compère (2012)). Our $J_2 \sim 0$ result does not contradict this statement, insofar as we analyze observational data and do not study the long term stability of the system. It shows that the estimation of the quadrupole term J_2 of the gravitational potential of Sylvia is not obvious, even impossible, given the available observational data, especially since a keplerian model provides the best-fit orbital solution. The discrepancy between our result and those of Fang et al. (2012) (who found a primary J_2 of 0.1), or those of Marchis et al. (2005a), reveals that the estimation of the J_2 term is strongly correlated with the orbit-fitting method. In all cases, very similar orbital solutions are obtained, and the same conclusion applies: Sylvia's system is ancient and in a very stable state.

5. Discussion

5.1. Interior of (87) Sylvia

The difference in J_2 from our dynamical analysis and as derived from the 3-D shape model implies that the assumption of an homogeneous mass distribution is not valid. The $J_2 \sim 0$ determined dynamically indicates a more concentrated mass distribution than the 3-D shape suggests, so that the primary could be differentiated with a dense core. The same result emerged from the analysis of the orbit of the 28 km-diameter satellite of (22) Kalliope, a 166 km-diameter M-

type asteroid. Vachier et al. (2012) suggested a differentiated internal structure for the primary of this binary system.

Recent developments (e.g., Ghosh et al. 2003) in thermal modeling of small solar system bodies showed that large enough (radius > 7 km) asteroids that accreted shortly after the Calcium-Aluminum inclusion formation (< 2.5 Myr), when ^{26}Al was still abundant, could have been molten internally. As they were cooling off, their internal composition became partially differentiated. Those models showed that these asteroids remained covered with a thick (up to tens of kilometers) un-melted relict crust (see a review on this mechanism and a thorough discussion in Weiss and Elkins-Tanton 2013).

Although we cannot conclude whether or not the internal structure of (87) Sylvia is differentiated, the very low J_2, perturbing the satellite's orbit, hints toward a dense core embedded into an irregularly shaped material. The lower density of the surrounding material may be related to composition or structure, e.g., a large macro-porosity generated by fractures.

5.2. Elongated shape of Romulus

The shape and size of Romulus was estimated in section 3.2 from the chords of an occultation, leading to a surface-area equivalent diameter $D_S = 23.1 \pm 0.7$ km (H = 12.1–12.3, assuming the same albedo as the primary of 0.0435, Tedesco et al. 2002), and an axis ratio $a/b \sim 2.7 \pm 0.3$ (assuming an ellipsoid). This is the second time the shape and size of a satellite of asteroid is measured using this technique. An occultation by Linus, satellite of the asteroid (22) Kalliope, gave a similar opportunity (Descamps et al. 2008), but the chords were too close to each other and the shape could only be approximated by a circular fit. In the case of Romulus, the positive and negative chords are sufficiently spread (Fig. 6) to give a meaningful constraint on its shape. The satellite appears extremely elongated, with the main axis of the silhouette ellipse oriented at $12^\circ \pm 4^\circ$ from the primary.

We searched in the *Asteroid Lightcurve Database* (Warner et al. 2009) containing the light-curves of 6160 small solar system bodies (including NEAs,

TNOs, main-belt and a few comets) those with an amplitude greater than 1.9 (corresponding to a size ratio ≥ 2.4) and found 15 asteroids, including 12 NEAs and 3 main-belt asteroids (Fig. 9). They are all significantly smaller than Romulus with a diameter varying from 20 m to 7.5 km. The largest, (44530) Horakova, has a light-curve poorly constrained with a period $P = 160$ h and a maximum light-curve amplitude $\Delta m \sim 2.7$, suggesting that it could be a tidally locked binary. Asteroid (1620) Geographos ($D = 1.6$ km, $\Delta m \sim 2.0$) is smaller but shows the same light-curve amplitude as Romulus. Moreover its shape is well-defined thanks to delay-Doppler radar observations (Ostro et al. 1996). Shape reconstruction from radar gives $a/b = 2.76 \pm 0.18$, similar to Romulus. Bottke et al. (1999) has shown by numerical simulations that tidal disruptions during a close encounter with a planet could produce the elongated shape of Geographos. Similarly, because Romulus is relatively close to the primary ($\sim$10 $\times$ Sylvia's radius), and could be a rubble-pile satellite which formed from fragments of a catastrophic collision on the parent body, its elongated shape may result of the tidal forces from the elongated and spinning primary. Another possibility is that Romulus is a bilobed satellite, relic of its formation by a low-relative speed encounter of two $\sim$10 km fragments of the parent body and captured in the gravitational field of the primary. An accurate modeling of the tidal evolution of the orbit and shape of the satellite could shed light on the internal stress and cohesive forces of the satellite.

6. Conclusion

This work demonstrates once again that the combination of adaptive-optics observations with light-curve photometric observations and stellar occultations is a powerful way to study multiple asteroid system. Similarly to our work on the triple asteroid (93) Minerva (Marchis et al. 2013b), we derive here the 3-D shape and size of Sylvia's primary and constrain its internal structure. The successful observation of the occultation by Romulus, the outer satellite of the system, provides the first well-constrained estimate of the shape of an asteroid's moon

which has an extreme elongation, likely due to the tides due to the primary. A follow-up of the orbits of Sylvia's moons based on additional AO observations, recorded with present AO systems and on the next generation of adaptive optics currently being designed for the Keck telescope (Wizinowich et al. 2010) or set up on new telescopes (e.g., LBTAO, see Esposito et al. 2011), will help to confirm the absence of precession indicative of a heterogeneous interior for this asteroid.

The analysis of the occultation chords recorded on January 6, 2013 does not reveal the presence of Remus, the inner satellite, because of a poor coverage of the Northern part of the occultation path (Fig. 2), where Remus was predicted to be located. No observer reported occultation events due to the presence of smaller, yet unknown, satellites around Sylvia's primary. From the timing accuracy of recorded light-curves (Tab. 4), we estimate that observers could have detected other satellites around Sylvia with a diameter larger than 2 km along the occultation chords (Fig. 2). For comparison, the upper limit of detection for the AO observations varies with the distance to the primary and the quality of the AO correction; typically a satellite larger than $\sim$5 km in diameter could have been detected if located at Remus' distance ($\sim 0.3''$). This is a clear illustration of the usefulness of occultation that help determining the multiplicity of an asteroid, even if it is far, too faint, and/or accompanied with a small moon undetectable by AO systems. As an example, the observation of an occultation by the Jupiter-trojan asteroid (911) Agamemnon in 2012 showed a deep brief secondary event that is likely due to a satellite of about 5 km (Timerson et al. 2013). Additional occultations involving (87) Sylvia are predicted in the near future. Table 8 lists a selection of events scheduled for the next 10 years, and their locations. In the future, we will continue to monitor the orbits of the satellites and deliver predictions of the moons' paths at the time of occultations.

Acknowledgments

We are grateful to all the observers for their efforts and for providing their

observations (Tab. 5). We appreciate the help of S. Preston (IOTA) who made available the prediction of the event, to H. Harris (UNSO/Flagstaff) and B. Owen (TMO) for providing last minute astrometric observations of the asteroid, to P. Descamps and *Les Makes* observatory (La Réunion island) for the astrometric measurements of the occulted star, to E. Frappa (Euraster), J. Lecacheux (LESIA/Observatoire de Paris) et al. to have organized the observational campaign and collected the observer reports. The work of F. Marchis was supported by the NASA grant NNX11AD62G. The work of J. Ďurech was supported by the grants GACR 209/10/0537 and P209/12/0229 of the Czech Science Foundation. We thank the C2PU team who gave us access to the data collected by the *Omicron* telescope of the *Centre Pédagogique Planète et Univers* (Observatoire de la Côte d'Azur, Calern site), as well as the TAROT observatory team who made available their robotic telescopes to record occultation events.

Table 1: Observational conditions of astrometric positions used for this work. References: a, b, c: reanalysis of data collected respectively by Brown et al. (2001); Storrs et al. (2001); Marchis et al. (2005a); d: astrometric positions reported in Fang et al. (2012); e, f: unpublished data acquired respectively by Marchis et al. and Carry et al.; g: this work

Date time (UTC)	V (mag)	D_{Earth} (au)	D_{Sun} (au)	Phase (°)	Elong. (°)	AM	Telescope	Ref.
2001-02-19 08:39:46.94	12.41	2.791595	3.755543	3.95	164.84	1.123	Keck/NIRC2	a
2001-02-19 10:03:57.89	12.41	2.791677	3.755554	3.96	164.81	1.014	Keck/NIRC2	a
2001-02-19 10:12:43.20	12.41	2.791686	3.755555	3.96	164.81	1.010	Keck/NIRC2	a
2001-02-20 09:39:27.36	12.41	2.793272	3.755729	4.08	164.33	1.027	Keck/NIRC2	a
2001-02-20 09:46:55.78	12.41	2.793281	3.755730	4.08	164.33	1.021	Keck/NIRC2	a
2001-02-23 13:40:12.58	12.45	2.800411	3.756284	4.58	162.37	-	HST/WFPC2	b
2004-07-25 10:22:17.76	12.14	2.410849	3.218312	12.82	135.39	1.205	VLT/NACO	c
2004-08-10 07:17:16.22	11.89	2.293127	3.217288	8.99	150.30	1.008	VLT/NACO	c
2004-08-29 07:18:19.30	11.64	2.230743	3.216817	5.05	163.73	1.115	VLT/NACO	c
2004-08-29 07:26:17.95	11.64	2.230739	3.216817	5.05	163.73	1.133	VLT/NACO	c
2004-08-29 08:46:08.83	11.64	2.230705	3.216817	5.04	163.75	1.445	VLT/NACO	c
2004-09-01 05:54:55.01	11.63	2.229630	3.216818	4.89	164.26	1.017	VLT/NACO	c
2004-09-01 06:03:55.01	11.63	2.229631	3.216818	4.89	164.26	1.024	VLT/NACO	c
2004-09-01 08:25:31.58	11.63	2.229646	3.216818	4.89	164.27	1.406	VLT/NACO	c
2004-09-03 07:09:06.34	11.63	2.230255	3.216830	4.90	164.22	1.148	VLT/NACO	c
2004-09-04 08:41:35.81	11.64	2.231039	3.216840	4.94	164.07	1.601	VLT/NACO	c
2004-09-05 04:09:27.94	11.64	2.231820	3.216849	4.99	163.89	1.015	VLT/NACO	c
2004-09-05 08:15:20.74	11.64	2.232024	3.216852	5.01	163.85	1.452	VLT/NACO	c
2004-09-06 03:50:04.13	11.65	2.233033	3.216863	5.08	163.61	1.027	VLT/NACO	c
2004-09-07 02:36:23.04	11.65	2.234453	3.216878	5.18	163.28	1.142	VLT/NACO	c
2004-09-07 09:24:57.31	11.65	2.234943	3.216883	5.21	163.17	2.283	VLT/NACO	c
2004-09-08 06:54:52.01	11.66	2.236557	3.216899	5.33	162.78	1.171	VLT/NACO	c
2004-09-11 04:51:29.95	11.69	2.243369	3.216966	5.80	161.20	1.006	VLT/NACO	c

Continued on next page

Table 1 – continued

Date time (UTC)	V (mag)	D_{Earth} (au)	D_{Sun} (au)	Phase (°)	Elong. (°)	AM	Telescope	Ref.
2004-09-13 03:25:24.10	11.72	2.249181	3.217022	6.17	159.92	1.020	VLT/NACO	c
2004-09-13 05:30:10.66	11.72	2.249465	3.217024	6.19	159.86	1.047	VLT/NACO	c
2004-09-14 03:49:52.03	11.73	2.252630	3.217054	6.39	159.19	1.003	VLT/NACO	c
2004-09-14 06:36:31.10	11.73	2.253047	3.217058	6.41	159.10	1.199	VLT/NACO	c
2004-09-14 06:44:34.08	11.73	2.253068	3.217058	6.41	159.10	1.225	VLT/NACO	c
2004-09-15 05:08:21.70	11.75	2.256499	3.217090	6.62	158.39	1.032	VLT/NACO	c
2004-09-15 05:16:22.94	11.75	2.256520	3.217090	6.62	158.39	1.042	VLT/NACO	c
2004-10-19 00:27:06.91	12.30	2.518403	3.219585	14.37	126.79	1.038	VLT/NACO	c
2004-10-20 00:08:28.03	12.31	2.529405	3.219697	14.54	125.85	1.057	VLT/NACO	c
2004-10-25 06:28:30.72	12.39	2.590441	3.220330	15.39	120.89	1.359	Keck/NIRC2	c
2004-11-02 07:34:37.34	12.51	2.690426	3.221417	16.43	113.48	1.428	Gemini/NIRI	c
2005-11-01 13:18:57.31	11.99	2.442235	3.394667	5.81	159.75	1.119	Gemini/NIRI	e
2005-11-06 08:19:53.76	11.90	2.426453	3.398045	4.28	165.18	1.304	Gemini/NIRI	e
2005-11-06 08:31:43.10	11.90	2.426431	3.398051	4.28	165.19	1.254	Gemini/NIRI	e
2005-12-20 10:01:06.82	12.35	2.598025	3.429626	10.23	141.83	1.201	Gemini/NIRI	e
2005-12-20 10:08:25.73	12.35	2.598075	3.429630	10.23	141.82	1.226	Gemini/NIRI	e
2005-12-21 08:42:06.05	12.36	2.607454	3.430311	10.46	140.78	1.041	Gemini/NIRI	e
2005-12-21 08:47:19.68	12.36	2.607491	3.430314	10.46	140.78	1.048	Gemini/NIRI	e
2006-01-01 10:43:07.10	12.56	2.731924	3.438370	12.90	128.79	1.765	Gemini/NIRI	e
2006-01-06 09:14:36.10	12.65	2.794520	3.441971	13.78	123.64	1.295	Gemini/NIRI	e
2006-01-06 09:20:56.26	12.65	2.794578	3.441974	13.78	123.64	1.323	Gemini/NIRI	e
2006-12-12 16:07:33.89	12.73	2.883229	3.670720	10.49	137.29	1.267	Keck/NIRC2	e
2010-07-27 05:23:00.04	11.64	2.259758	3.253753	4.03	166.98	1.027	VLT/SINFONI	e
2010-08-15 08:37:41.66	11.94	2.331035	3.244915	8.95	150.09	1.639	Gemini/NIRI	e
2010-08-25 08:28:46.85	12.10	2.403504	3.240567	11.54	140.07	1.662	Gemini/NIRI	e
2010-08-28 08:22:10.27	12.15	2.429262	3.239301	12.25	137.09	1.671	Gemini/NIRI	e
2010-08-30 05:57:29.00	12.18	2.446480	3.238507	12.68	135.21	1.647	VLT/NCAO	f
2010-09-01 08:27:56.74	12.22	2.466323	3.237635	13.13	133.14	1.717	Gemini/NIRI	e

Continued on next page

Table 1 – continued

Date time (UTC)	V (mag)	D_{Earth} (au)	D_{Sun} (au)	Phase (°)	Elong. (°)	AM	Telescope	Ref.
2010-09-02 06:34:03.36	12.23	2.475252	3.237257	13.33	132.24	1.694	Gemini/NIRI	e
2011-10-07 02:37:58.08	11.68	2.277797	3.251690	4.40	165.53	1.357	VLT/NACO	d
2011-11-06 02:03:15.84	11.99	2.376961	3.266863	8.84	149.55	1.088	VLT/NACO	d
2011-11-08 03:05:36.96	12.03	2.392516	3.267956	9.38	147.45	1.066	VLT/NACO	d
2011-11-10 01:04:56.64	12.06	2.408016	3.268988	9.88	145.48	1.149	VLT/NACO	d
2011-11-15 00:36:51.84	12.15	2.452228	3.271698	11.12	140.34	1.163	VLT/NACO	d
2011-11-16 01:07:06.24	12.17	2.461963	3.272259	11.36	139.28	1.103	VLT/NACO	d
2011-11-20 01:06:14.40	12.24	2.502190	3.274473	12.27	135.18	1.086	VLT/NACO	d
2011-12-15 05:06:34.56	12.65	2.816075	3.289009	16.26	110.50	1.104	Keck/NIRC2	d
2011-12-15 05:29:28.32	12.65	2.816297	3.289018	16.27	110.48	1.087	Keck/NIRC2	d
2011-12-15 06:28:30.72	12.65	2.816873	3.289043	16.27	110.44	1.098	Keck/NIRC2	d
2011-12-16 04:30:17.28	12.66	2.829790	3.289592	16.36	109.59	1.147	Keck/NIRC2	d
2011-12-16 06:01:26.40	12.67	2.830682	3.289630	16.36	109.53	1.084	Keck/NIRC2	d
2011-12-17 06:16:33.60	12.68	2.844990	3.290237	16.45	108.60	1.093	Keck/NIRC2	d
2011-12-18 04:43:58.08	12.69	2.858315	3.290799	16.53	107.74	1.114	Keck/NIRC2	d
2011-12-18 04:53:02.40	12.69	2.858404	3.290803	16.53	107.73	1.104	Keck/NIRC2	d
2013-01-06 01:38:14.18	12.30	2.654901	3.581037	6.01	157.56	1.438	Occ. data	g

Table 2: List of **Remus** astrometric observations (X_o, Y_o) collected from February 2001 to December 2011. The computed positions (X_c, Y_c) were obtained with the orbital elements published in this paper. The uncertainty σ of astrometric positions is taken as the instrument plate scale. References: c.f. Tab. 1.

Date time (UTC)	X_o (arcsec)	Y_o (arcsec)	X_c (arcsec)	Y_c (arcsec)	X_{O-C} (arcsec)	Y_{O-C} (arcsec)	σ (mas)	Ref.
2001-02-23T13:40:12.58	0.3448	0.0290	0.3347	0.0341	0.0101	-0.0051	40.2	b
2004-08-10T07:19:16.00	0.3952	0.0136	0.4046	0.0032	-0.0094	0.0104	13.3	c
2004-09-01T05:57:01.00	0.2074	-0.0881	0.2379	-0.0936	-0.0306	0.0054	13.3	c
2004-09-01T06:05:55.00	0.2216	-0.0904	0.2278	-0.0948	-0.0063	0.0044	13.3	c
2004-09-03T07:11:06.00	-0.2199	0.1030	-0.2082	0.0981	-0.0117	0.0049	13.3	c
2004-09-05T04:11:28.00	0.4052	-0.0507	0.4007	-0.0489	0.0045	-0.0018	13.3	c
2004-09-07T02:38:22.00	-0.4350	0.0009	-0.4182	0.0029	-0.0168	-0.0020	13.3	c
2004-09-08T06:56:51.00	-0.2461	-0.0620	-0.2451	-0.0760	-0.0010	0.0141	13.3	c
2004-09-13T03:27:24.00	0.3693	0.0385	0.3786	0.0298	-0.0093	0.0087	13.3	c
2004-09-13T05:32:11.00	0.4086	-0.0136	0.4187	-0.0135	-0.0101	-0.0001	13.3	c
2004-09-14T03:51:51.00	-0.1897	0.1251	-0.1793	0.1050	-0.0105	0.0202	13.3	c
2004-09-15T05:10:21.96	-0.3956	0.0002	-0.4028	-0.0109	0.0073	0.0110	13.3	c
2004-09-15T05:18:22.00	-0.3944	-0.0012	-0.4055	-0.0081	0.0112	0.0069	13.3	c
2010-08-15T08:37:52.00	0.2289	0.1330	0.2249	0.1351	0.0040	-0.0021	13.3	e
2010-08-28T08:23:47.00	-0.3366	-0.0499	-0.3417	-0.0461	0.0052	-0.0038	13.3	e
2010-09-01T08:29:10.00	-0.2675	-0.1232	-0.2695	-0.0989	0.0020	-0.0243	13.3	e
2010-09-02T06:35:15.00	0.3820	-0.1122	0.3555	-0.1057	0.0265	-0.0066	13.3	e
2011-10-07T02:37:58.08	-0.3910	-0.0340	-0.4017	-0.0277	0.0107	-0.0063	13.3	d
2011-11-08T03:05:36.96	0.2180	0.0570	0.2218	0.0283	-0.0038	0.0287	13.3	d
2011-11-10T01:04:56.64	-0.3420	0.0020	-0.3564	-0.0233	0.0144	0.0253	13.3	d
2011-11-16T01:07:06.24	0.3810	0.0180	0.3827	0.0126	-0.0017	0.0054	13.3	d
2011-12-15T05:06:34.56	-0.3410	-0.0110	-0.3346	-0.0097	-0.0064	-0.0013	9.9	d
2011-12-15T05:29:28.32	-0.3420	-0.0150	-0.3347	-0.0121	-0.0073	-0.0029	9.9	d

Continued on next page

Table 2 – continued

Date time (UTC)	X_o (arcsec)	Y_o (arcsec)	X_c (arcsec)	Y_c (arcsec)	X_{O-C} (arcsec)	Y_{O-C} (arcsec)	σ (mas)	Ref.
2011-12-15T06:28:30.72	-0.3250	-0.0120	-0.3266	-0.0179	0.0016	0.0059	9.9	d
2011-12-17T06:16:33.60	0.3480	0.0350	0.3314	0.0116	0.0166	0.0234	9.9	d

Table 3: List of **Romulus** astrometric observations (X_o, Y_o) collected from February 2001 to December 2011. The computed positions (X_c, Y_c) were obtain with the orbital elements published in this paper. The uncertainty σ of astrometric positions is taken as the instrument plate scale. References: c.f. Tab. 1.

Date time (UTC)	X_o (arcsec)	Y_o (arcsec)	X_c (arcsec)	Y_c (arcsec)	X_{O-C} (arcsec)	Y_{O-C} (arcsec)	σ (mas)	Ref.
2001-02-19T08:41:16.998	0.3401	0.2101	0.3589	0.2108	-0.0189	-0.0007	9.9	a
2001-02-19T10:04:18.001	0.2806	0.2190	0.3017	0.2178	-0.0211	0.0012	9.9	a
2001-02-19T10:13:03.002	0.2815	0.2421	0.2954	0.2185	-0.0139	0.0236	9.9	a
2001-02-20T09:40:55.997	-0.6242	0.0306	-0.6273	0.0337	0.0031	-0.0031	9.9	a
2001-02-20T09:48:26.003	-0.6161	0.0394	-0.6294	0.0317	0.0132	0.0077	9.9	a
2001-02-23T13:40:11.997	-0.2532	0.1957	-0.2688	0.1861	0.0156	0.0096	40.2	b
2004-07-25T10:22:42.003	-0.7657	-0.0070	-0.7530	-0.0084	-0.0128	0.0015	13.3	c
2004-08-10T07:19:16.000	0.3738	0.1392	0.3877	0.1408	-0.0139	-0.0016	13.3	c
2004-08-29T07:20:19.003	0.7728	-0.1082	0.7916	-0.0946	-0.0188	-0.0136	13.3	c
2004-08-29T07:28:17.996	0.7940	-0.1065	0.7890	-0.0963	0.0050	-0.0102	13.3	c
2004-08-29T08:48:08.003	0.7434	-0.1190	0.7584	-0.1132	-0.0150	-0.0058	13.3	c
2004-09-01T05:57:00.996	0.5454	0.1366	0.5514	0.1363	-0.0060	0.0003	13.3	c
2004-09-01T06:05:55.000	0.5545	0.1330	0.5581	0.1346	-0.0036	-0.0016	13.3	c
2004-09-01T08:27:37.995	0.6583	0.1065	0.6552	0.1057	0.0031	0.0007	13.3	c
2004-09-03T07:11:05.999	-0.7498	-0.0610	-0.7497	-0.0599	-0.0001	-0.0011	13.3	c
2004-09-04T08:43:35.999	-0.1603	0.1950	-0.1423	0.2135	-0.0180	-0.0185	13.3	c
2004-09-05T04:11:27.997	0.7851	0.0490	0.7862	0.0433	-0.0012	0.0057	13.3	c
2004-09-05T08:17:20.002	0.8362	-0.0192	0.8363	-0.0191	-0.0001	-0.0002	13.3	c
2004-09-06T03:52:03.999	0.1661	-0.2058	0.1858	-0.2126	-0.0197	0.0068	13.3	c
2004-09-07T02:38:22.004	-0.8307	0.0053	-0.8216	0.0046	-0.0091	0.0007	13.3	c
2004-09-07T09:26:55.999	-0.7914	0.1163	-0.7785	0.1060	-0.0129	0.0104	13.3	c
2004-09-08T06:56:51.002	0.2542	0.1941	0.2694	0.1926	-0.0152	0.0015	13.3	c
2004-09-11T04:53:29.996	-0.6726	0.1650	-0.6542	0.1600	-0.0184	0.0050	13.3	c

Continued on next page

Table 3 – continued

Date time (UTC)	X_o (arcsec)	Y_o (arcsec)	X_c (arcsec)	Y_c (arcsec)	X_{O-C} (arcsec)	Y_{O-C} (arcsec)	σ (mas)	Ref.
2004-09-13T03:27:24.001	0.5571	-0.1980	0.5477	-0.1852	0.0094	-0.0128	13.3	c
2004-09-13T05:32:11.002	0.4478	-0.1852	0.4482	-0.2004	-0.0004	0.0153	13.3	c
2004-09-14T03:51:50.996	-0.7220	-0.0725	-0.7136	-0.0758	-0.0084	0.0033	13.3	c
2004-09-14T06:38:29.999	-0.7710	-0.0361	-0.7811	-0.0330	0.0101	-0.0031	13.3	c
2004-09-14T06:46:34.003	-0.7829	-0.0314	-0.7836	-0.0309	0.0007	-0.0005	13.3	c
2004-09-15T05:18:22.003	-0.2080	0.2215	-0.2048	0.2204	-0.0032	0.0011	13.3	c
2004-10-19T00:29:36.003	0.7423	-0.0400	0.7424	-0.0392	-0.0001	-0.0008	13.3	c
2004-10-20T00:10:57.996	-0.0891	-0.1748	-0.0993	-0.1846	0.0101	0.0098	13.3	c
2004-10-25T06:29:31.001	-0.1298	0.1851	-0.1333	0.1891	0.0034	-0.0040	9.9	c
2004-11-02T07:35:11.999	0.6486	0.0460	0.6243	0.0427	0.0244	0.0033	22.0	c
2005-11-01T13:20:57.001	0.0015	-0.2670	-0.0046	-0.2581	0.0061	-0.0089	22.0	e
2005-11-06T08:20:06.002	0.6840	0.1901	0.6911	0.1814	-0.0071	0.0088	22.0	e
2005-11-06T08:32:42.996	0.6914	0.1739	0.6862	0.1844	0.0051	-0.0105	22.0	e
2005-12-20T10:01:09.001	0.2384	0.2573	0.2450	0.2594	-0.0066	-0.0021	22.0	e
2005-12-20T10:10:25.996	0.2434	0.2434	0.2375	0.2596	0.0059	-0.0162	22.0	e
2005-12-21T08:42:09.002	-0.7005	0.0065	-0.6844	0.0035	-0.0161	0.0030	22.0	e
2005-12-21T08:48:50.002	-0.6704	0.0129	-0.6860	0.0014	0.0156	0.0115	22.0	e
2006-01-01T10:44:37.003	-0.6687	-0.0559	-0.6808	-0.0677	0.0121	0.0118	22.0	e
2006-01-06T09:14:37.996	0.4125	-0.1554	0.4061	-0.1544	0.0063	-0.0009	22.0	e
2006-01-06T09:22:55.997	0.4112	-0.1418	0.4113	-0.1525	-0.0000	0.0106	22.0	e
2006-12-12T16:09:34.001	0.5659	0.1796	0.5353	0.1994	0.0306	-0.0199	9.9	e
2010-07-27T05:23:00.040	0.3900	0.2950	0.3719	0.3024	0.0181	-0.0074	12.5	e
2010-08-15T08:37:51.997	0.6981	-0.2980	0.6827	-0.2803	0.0155	-0.0177	22.0	e
2010-08-25T08:30:23.002	0.4274	0.2690	0.4061	0.2778	0.0213	-0.0089	22.0	e
2010-08-28T08:23:46.996	-0.4167	0.3680	-0.3989	0.3656	-0.0178	0.0024	22.0	e
2010-08-30T05:57:28.998	0.3225	-0.3714	0.3252	-0.3766	-0.0027	0.0052	13.3	f
2010-09-01T08:29:10.003	0.0744	0.3535	0.0584	0.3638	0.0161	-0.0102	22.0	e

Continued on next page

Table 3 – continued

Date time (UTC)	X_o (arcsec)	Y_o (arcsec)	X_c (arcsec)	Y_c (arcsec)	X_{O-C} (arcsec)	Y_{O-C} (arcsec)	σ (mas)	Ref.
2010-09-02T06:35:15.002	0.7748	-0.1153	0.7493	-0.1171	0.0256	0.0018	22.0	e
2011-10-07T02:37:58.002	-0.6980	-0.0720	-0.7047	-0.0615	0.0067	-0.0105	13.3	d
2011-11-06T02:03:15.001	0.3680	-0.0190	0.3771	-0.0250	-0.0091	0.0060	13.3	d
2011-11-08T03:05:36.000	-0.6060	0.0150	-0.6088	0.0054	0.0028	0.0096	13.3	d
2011-11-10T01:04:56.000	0.6430	0.0120	0.6741	0.0015	-0.0311	0.0105	13.3	d
2011-11-15T00:36:51.001	-0.1770	0.0460	-0.1824	0.0373	0.0054	0.0087	13.3	d
2011-11-16T01:07:05.998	-0.6700	-0.0450	-0.6832	-0.0423	0.0132	-0.0027	13.3	d
2011-11-20T01:06:14.002	-0.3550	-0.0350	-0.3609	-0.0527	0.0059	0.0177	13.3	d
2011-12-15T05:06:33.998	-0.5680	-0.0570	-0.5736	-0.0483	0.0056	-0.0087	9.9	d
2011-12-15T05:29:28.000	-0.5680	-0.0630	-0.5644	-0.0495	-0.0036	-0.0135	9.9	d
2011-12-15T06:28:30.002	-0.5390	-0.0460	-0.5387	-0.0523	-0.0003	0.0063	9.9	d
2011-12-16T04:30:17.003	0.3910	-0.0370	0.3829	-0.0392	0.0081	0.0022	9.9	d
2011-12-16T06:01:26.002	0.4460	-0.0160	0.4385	-0.0334	0.0075	0.0174	9.9	d
2011-12-17T06:16:33.003	0.4150	0.0820	0.4080	0.0612	0.0070	0.0208	9.9	d
2011-12-18T04:43:58.002	-0.5280	0.0260	-0.5306	0.0200	0.0026	0.0060	9.9	d
2011-12-18T04:53:02.002	-0.5210	0.0190	-0.5346	0.0193	0.0136	-0.0003	9.9	d
2013-01-06T01:38:14.000	0.5930	-0.1130	0.5898	-0.1041	0.0032	-0.0089	4.5	g

Table 4: Timings and uncertainties of the occultation of TYC2 1856-00745-1 by (87) Sylvia on January 6, 2013 (source: *Euraster* Web site). Notes: [a] Target: S for Sylvia, R for Romulus, [b] Measurement uncertainty not provided by the observer, [c] No absolute timing due to technical problem; the only reliable data is the duration of the event, and the delay between the two disappearance times, which is 97.10 ±0.03 sec.

T [a]	Name	Duration (s)	Disp. Time (h:m:s ±s)	Reap. Time (h:m:s ±s)	Offset (s)
S	A. Carbognani	17.70	01:37:33.30 ±0.28	01:37:51.00 ±0.28	
S	S. Bolzoni	18.20	01:37:29.15 ±0.30	01:37:47.35 ±0.20	
S	S. Sposetti, A. Manna	25.34	01:37:26.21 ±0.03	01:37:51.55 ±0.04	
S	V. Fristot	21.50	01:37:30.70 ±0.20	01:37:52.20 ±0.20	
S	A. Figer	26.20	01:37:22.80 ±0.60	01:37:49.00 ±0.80	
S	M. Bretton	18.10	01:37:34.50 ±0.0 [b]	01:37:52.60 ±0.0 [b]	-3.8
S	J. Lecacheux	4.06	01:37:37.16 ±0.08	01:37:41.22 ±0.10	
S	P. Tanga	19.19	00:00:00.00 ±0.02 [c]	00:00:19.19 ±0.02 [c]	
S	M. Devogele et al.	12.77	01:37:26.73 ±0.08	01:37:39.50 ±0.08	
S	E. Frappa, A. Klotz	12.90	01:37:26.60 ±0.10	01:37:39.50 ±0.10	
S	L. Brunetto et al.	7.12	01:37:29.53 ±0.02	01:37:36.65 ±0.02	
S	V. Metallinos	24.60	01:36:20.73 ±0.05	01:36:45.33 ±0.05	
R	P. Tanga	1.96	00:00:97.10 ±0.03 [c]	00:00:99.06 ±0.03 [c]	
R	P. Dubreuil	1.70	01:38:57.60 ±2.00	01:38:59.30 ±2.00	0.5
R	M. Devogele et al.	0.56	01:39:00.85 ±0.08	01:39:01.41 ±0.08	
R	E. Frappa, A. Klotz	0.48	01:39:00.73 ±0.08	01:39:01.21 ±0.08	

Table 5: Observers of the occultation of TYC2 1856-00745-1 by (87) Sylvia on January 6, 2013 (source: *Euraster* Web site). Method is: <optic>, <acquisition>, <time source>, with abbreviations: L: Refractor, M: Reflector, CCD: CCD or CMOS imaging, VID: video recording, VIS: visual, GPS++: GPS one Pulse Per Second, PHONE: Phone time signal (wired phone), RAD: Radio time signal, RAD+: Intermittent radio controlled clock updated just before event, NTP: Network Time Protocol. Coordinates datum: W = WGS84; Altitude datum: W = WGS84, S = Mean Sea Level

Name	Method	Longitude (° ′ ″)	Latitude (° ′ ″)	Alt. (m)	Datum
S. Sposetti (CH)	M400, VID	E 09 01 26.5	N 46 13 53.2	260	WS
C. Gualdoni (IT)	M250, VID	E 09 06 01.0	N 45 48 18.0	255	WS
A. Carbognani (IT)	M810, CCD, NTP	E 07 28 42.0	N 45 47 23.5	1678	WS
S. Bolzoni (IT)	M300, VIS, RAD+	E 08 09 59.8	N 45 21 57.0	195	WS
U. Quadri et al. (IT)	M250, CCD	E 10 07 49.5	N 45 19 32.4	63	WS
S. Sposetti, A. Manna (IT)	M200, VID, GPS++	E 07 18 01.3	N 45 07 34.1	585	WS
V. Fristot (FR)	L102, CCD, NTP	E 05 16 35.4	N 44 41 35.5	390	WS
A. Figer (FR)	L68 , CCD, PHONE	E 06 40 54.0	N 44 34 24.0	1845	WS
M. Bretton (FR)	M820, VIS, RAD	E 05 30 54.4	N 44 24 29.9	810	WS
J.-L. Penninckx (FR)	M400, VIS	E 04 22 45.8	N 44 07 51.5	245	
C. Peguet (FR)	M350, VIS	E 05 00 09.0	N 44 07 31.8	94	WS
L. Bernasconi (FR)	M500, CCD	E 05 11 11.2	N 44 01 17.5	330	WS
J. Lecacheux (FR)	L130, VID, GPS++	E 06 01 15.3	N 43 58 48.6	720	WS
E. Frappa et al. (FR)	L61, VID	E 05 58 33.4	N 43 56 07.9	460	WS
L. Arnold (FR)	M205, CCD	E 05 42 48.4	N 43 55 00.7	551	WS
E. Frappa (FR)	M203, VID	E 06 00 23.0	N 43 51 51.9	628	WS
G. Brabant (FR)	M200, VID	E 04 54 47.5	N 43 47 48.8	53	WS
P. Tanga (FR)	M356, CCD	E 07 15 47.2	N 43 47 22.2	385	WS
P. Dubreuil (FR)	M203, CCD	E 07 14 30.6	N 43 46 58.5	480	WS
D. Verilhac (FR)	M210, VID	E 04 53 35.1	N 43 46 01.0	115	WS

Continued on next page

Table 5 – continued

Name	Method	Longitude (° ′ ″)	Latitude (° ′ ″)	Alt. (m)	Datum
M. Devogele et al. (FR)	M1000 ,VID, GPS++	E 06 55 21.8	N 43 45 13.5	1280	WS
E. Frappa, A. Klotz (FR)	M250, CCD, GPS++	E 06 55 25.1	N 43 45 07.3	1270	WS
O. Lecacheux (FR)	L61, VID, GPS++	E 05 30 00.0	N 43 41 31.6	214	WS
R. Poncy (FR)	M400, CCD	E 03 56 24.0	N 43 38 50.0	54	WS
L. Brunetto et al. (FR)	M406, VID, GPS++	E 07 04 18.4	N 43 36 15.7	130	WS
D. Albanese (FR)	M280, CCD	E 06 39 04.9	N 43 29 45.9	43	WS
F. Colas (FR)	M1050, CCD	E 00 08 32.5	N 42 56 10.9	2871	WS
J. Lopez (ES)	M200, VID	E 02 59 50.5	N 42 15 00.2	19	W
C. Perello, A. Selva (ES)	M500, VID	E 02 05 24.6	N 41 33 00.2	224	WS
R. Casas (ES)	M200, VID	E 02 07 14.3	N 41 32 22.1	165	WS
H. Pallares (ES)	M280, VIS	E 04 14 28.1	N 39 49 12.7	19	W
V. Metallinos (GR)	L130, VID, GPS++	E 19 52 23.3	N 39 38 07.4	2	WS

Table 6: Physical parameters of Sylvia's primary derived using KOALA algorithm.

Parameter	Value	Uncertainty (3-σ)
Spin axis ecliptic J2000 longitude	70°	±9°
Spin axis ecliptic J2000 latitude	69°	±3°
Sidereal rotation period	5.183640 h	$\pm 3 \times 10^{-6}$ h
Volume-equivalent diameter D_V	273 km	±10 km
Quadrupole term J_2	0.024	0.015 – 0.040
Volume	1.07×10^7 km^3	$\pm 0.09 \times 10^7$ km^3
Surface area	2.47×10^5 km^2	$\pm 0.15 \times 10^5$ km^2
Maximum dimensions along the principal axes		
a	193 km	180 – 210 km
b	129 km	127 – 160 km
c	124 km	115 – 150 km
Dynamically equivalent ellipsoid		
a/c	1.46	1.30 – 1.75
b/c	1.07	1.02 – 1.20

Table 7: Remus and Romulus best-fit orbital elements (EQJ2000) obtained using our *Genoid-Kepler* algorithm (orbital period P, semi-major axis a, eccentricity e, inclination i, longitude of the ascending node Ω, argument of the pericenter ϖ, time of pericenter t_p), and derived parameters (primary mass M, primary density ρ, ecliptic J2000 coordinates of the orbital pole λ_p, β_p). Errors are given at 3-σ.

Element	Remus		Romulus	
P (day)	1.356654	$\pm 5.9 \times 10^{-5}$	3.641191	$\pm 1.98 \times 10^{-4}$
a (km)	684.4	$\pm$ 109.7	1351.7	$\pm$ 151.0
e	0.0	$\pm$ 0.05	0.007	$\pm$ 0.047
i (deg)	8.6	$\pm$ 13.5	8.3	$\pm$ 7.7
Ω (deg)	93.0	$\pm$ 48.0	93.6	$\pm$ 20.1
ϖ (deg)	187.9	$\pm$ 52.1	109.1	$\pm$ 23.6
t_p (JD)	2455594.58824	$\pm$ 0.158	2455596.41837	$\pm$ 0.202
Derived parameters				
M (10^{19} kg)	1.380	$\pm$ 0.669	1.476	$\pm$ 0.497
ρ (g.cm^{-3})	1.29	$\pm$ 0.59	1.38	$\pm$ 0.44
λ_p, β_p (deg)	70, +65	$\pm$ 30, 9	70, +65	$\pm$ 17, 4

Table 8: Selection of stellar occultations by (87) Sylvia scheduled for the next 10 years. Tycho-2 stars; Mean epoch: approximated time of event; m_*: magnitude of the target star; Δm: magnitude drop, Δt: estimated maximum duration of the event, Location: main area of visibility.

Mean epoch (UTC)	Star TYC2	m_* mag	Δm mag	Δt (s)	Location
2016-01-30 07:22	6226 01275	12.1	1.6	8.0	Brazil
2016-06-22 23:54	6815 03609	11.6	0.6	20.5	Chile, Argentina, South Africa, Madagascar
2016-08-16 23:36	6817 01360	12.6	1.1	44.6	Chile, Paraguay, Brazil (South)
2016-11-03 23:17	6854 00301	10.6	1.4	7.2	Chile, Argentina, Brazil (South)
2019-10-15 08:11	1931 01512	9.9	2.0	14.1	Chile, Argentina, Brazil (South), South Africa
2019-10-20 06:08	1932 00479	12.0	1.9	15.8	Spain, France (South), Italy, Greece
2019-10-29 23:45	1932 00469	10.0	1.9	21.0	Spain, France, Italy, Germany, Poland
2023-07-06 08:01	7442 01392	11.9	1.0	22.2	Mexico, USA (East), Canada (East)

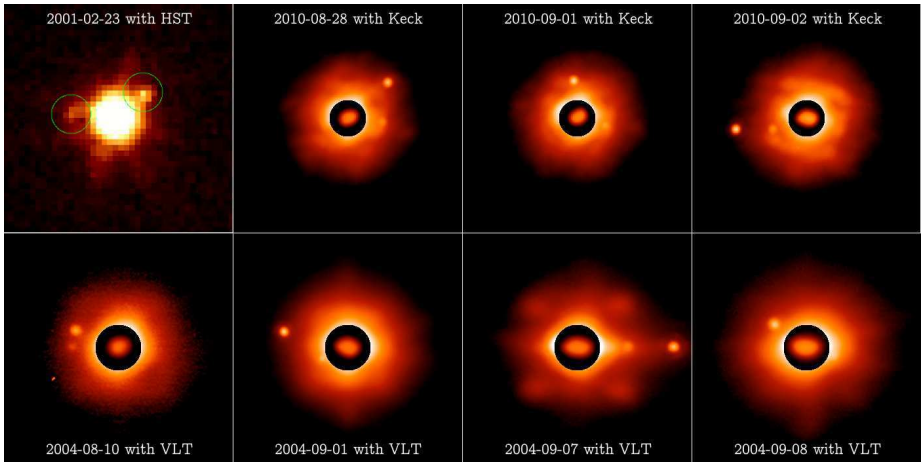


Figure 1: Sample of observations of the triple asteroid (87) Sylvia taken with the HST/WFPC2, W.M. Keck AO and VLT/NACO revealing the two satellites and the well resolved primary (angular size $\sim 0.2''$). The high levels of intensity showing the irregular shape of the primary are shown in the central circle. North is up, and East is left. The plate scale is 40.2 mas for the HST/WFPC2, 9.9 mas for the Keck/NIRC2, and 13.3 mas for the VLT/NACO observations.

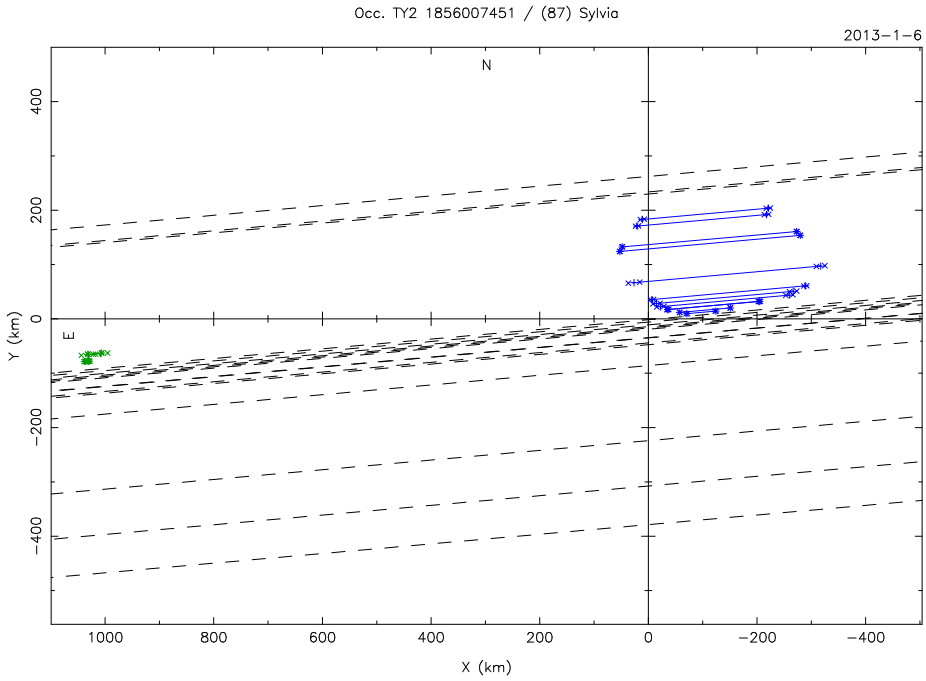


Figure 2: Observed chords (blue segments) of the January 6, 2013 occultation of TYC2 1856-00745-1 by (87) Sylvia and its satellite Romulus (green leftmost segments). The black dashed lines represent negative observations.

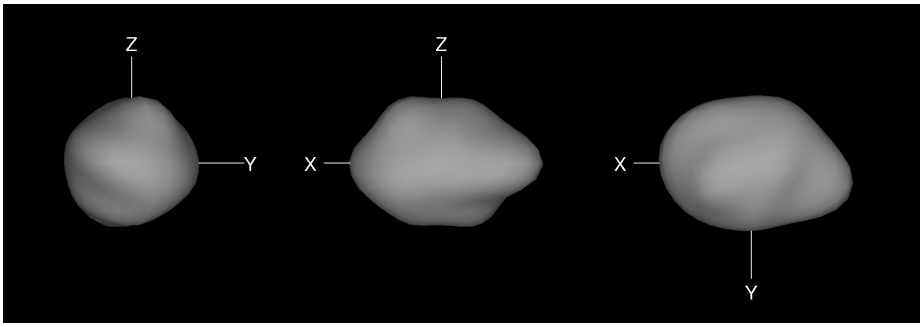


Figure 3: One of the best-fit models of Sylvia's primary (equatorial, equatorial, and polar view) derived from the combination of light-curve inversion, AO, and occultation data.

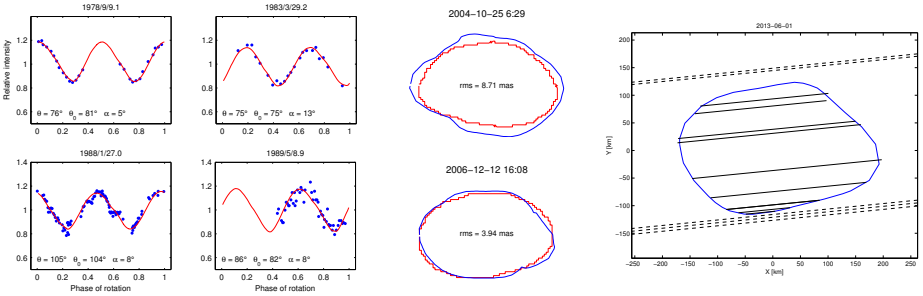


Figure 4: Result of the fit of Sylvia's 3-D shape compared to a sample of light-curves, image profiles, and occultation chords. The measured light-curves (points) are compared with the model (solid curves). The viewing and illumination geometry is described by the latitudes θ and θ_0 of the sub-Earth and sub-solar point, respectively, and by the solar phase angle α. The observed contours of AO images and the corresponding projections of the model (smooth blue curves) are plotted in the second panel. In the third panel, occultation chords and the model outline are shown. The dashed lines are negative observations.

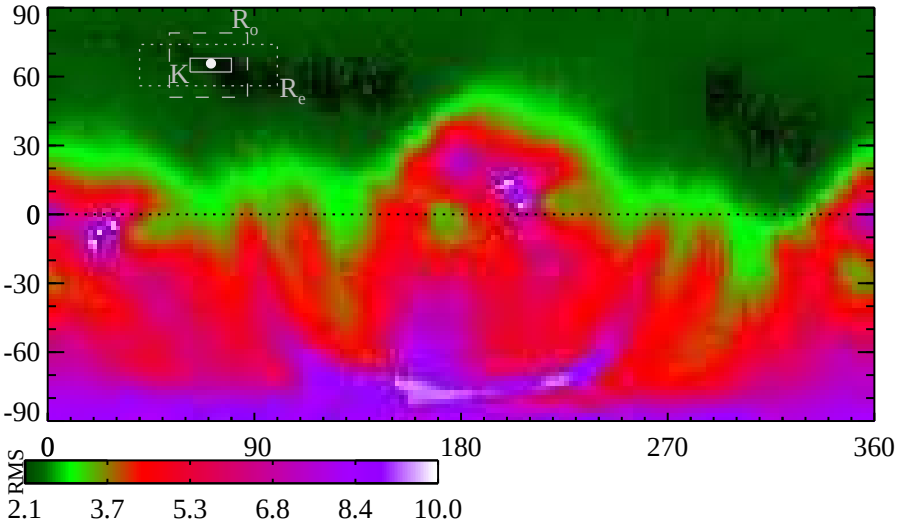


Figure 5: RMS residuals between the synthetic and observed lightcurves for spin-vector coordinates covering the entire celestial sphere with grid interval of 2°. The white points shows the best-fit spin solution (70°, +69°), and the three rectangles correspond to the 3–σ confidence interval provided by KOALA, the orbital pole of Romulus, and Remus, respectively, outside which spin-vectors coordinates are unlikely.

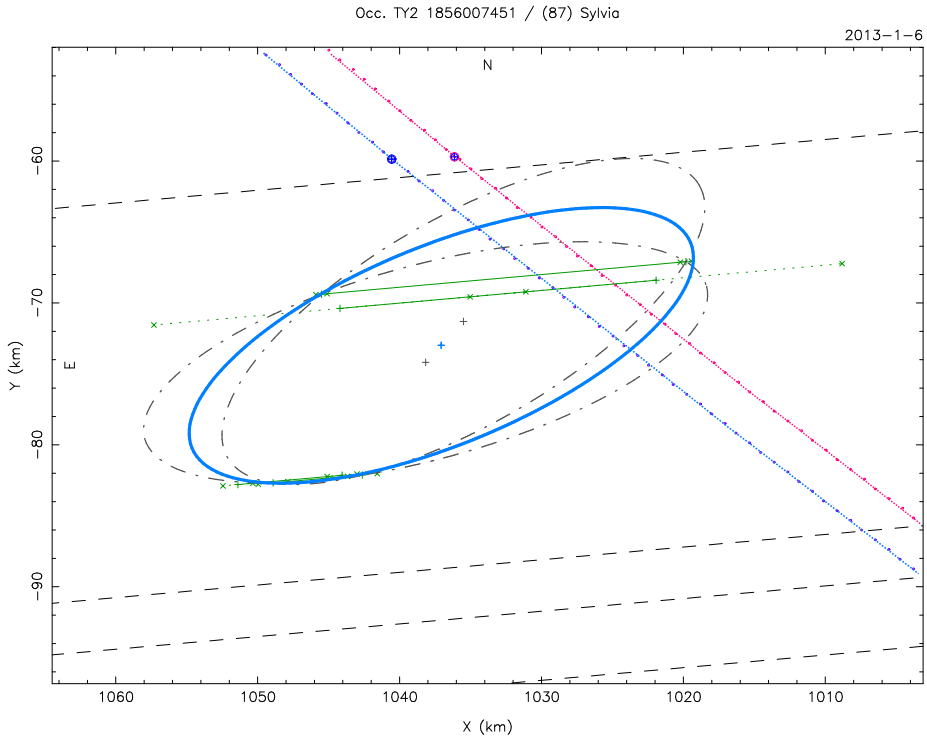


Figure 6: Romulus conic model fitted on the observed chords (green segments). The (blue) ellipse is the mean model, and the two dashed ellipses are the two extreme solutions at 3–σ. The dashed black lines are negative observations (northern one by V. Fristot). The blue (leftmost) and red lines show the predicted orbit of Romulus projected into the occultation plane, respectively based on the previous and the new orbital models. The two marks on these lines (located at $y \sim -60$ km) enlighten the predicted positions of Romulus at the epoch of occultation.

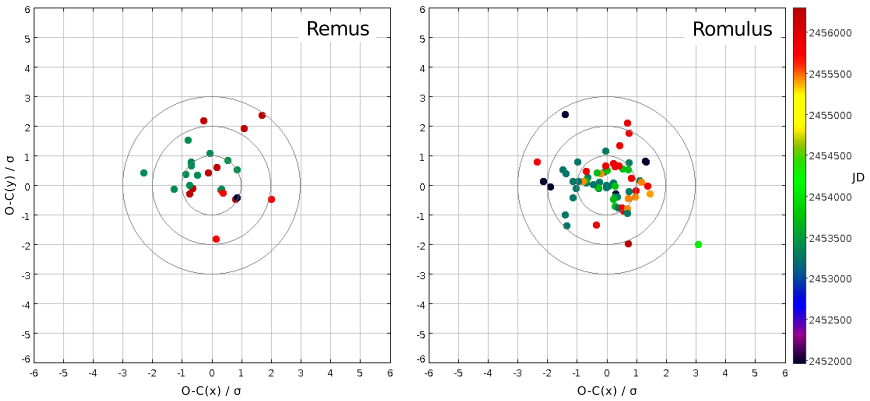


Figure 7: Mean residuals (observed minus computed satellite – primary positions) normalized by the positional uncertainty σ for Remus and Romulus.

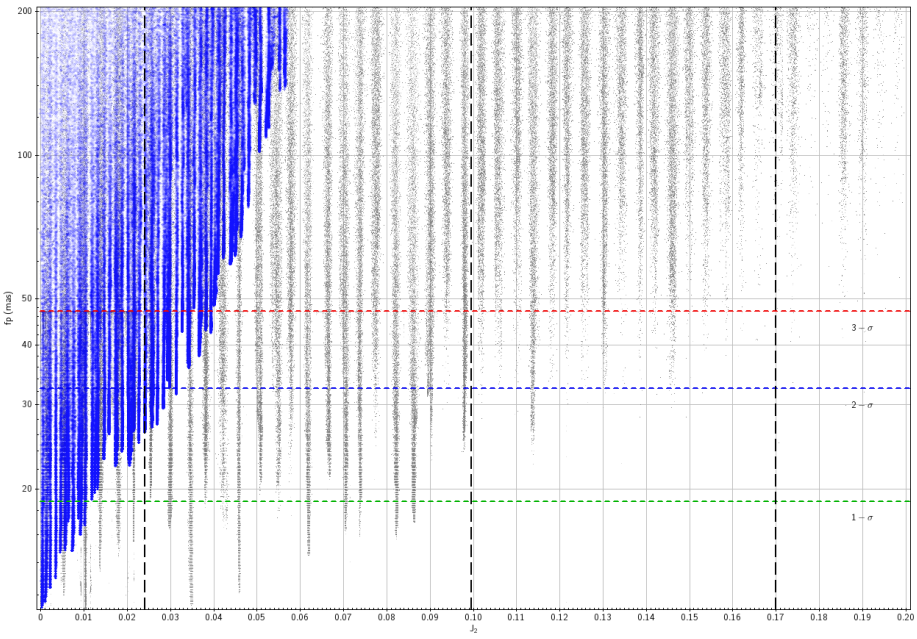


Figure 8: Result of the examination of the quadrupole term J_2 with *Genoid-ANIS*. The gray dots are all solutions. The (blue) biggest points show the solutions for which the orbital pole covers a range of 20° around the best-fit spin solution of the primary (i.e., rectangles in Fig. 5). The (green, blue, red) horizontal dashed lines correspond, respectively, to 1–σ, 2–σ and 3–σ thresholds. The three vertical lines indicate the J_2 values estimated, from left to right, from the 3-D shape model (see Sec. 3.1), by Fang et al. (2012) and by Marchis et al. (2005a). The best candidate solutions are obtained for $J_2 \to 0$.

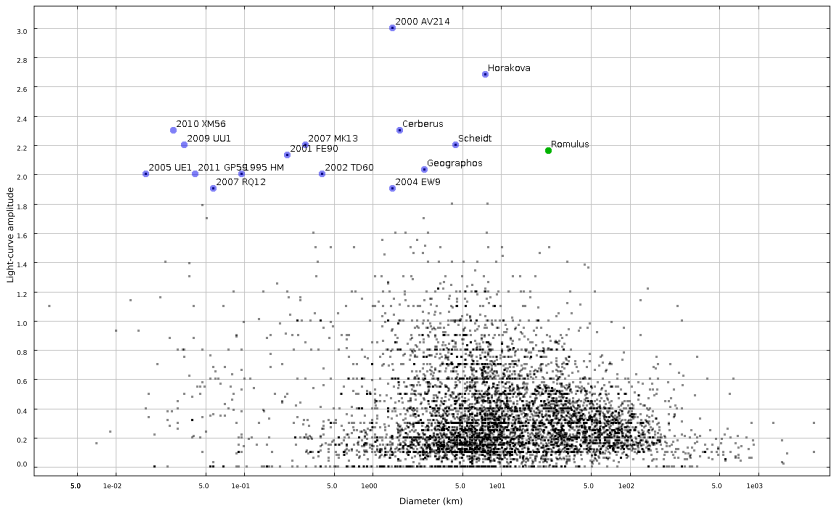


Figure 9: Distribution of 6160 asteroids based on light-curve amplitude versus diameter (source of data: *Asteroid Lightcurve Database*, Warner et al. 2009). High amplitude objects are labeled. We added Romulus for comparison, with $D_S = 23.1$ km and an amplitude estimated to 2.16 (corresponding to an axis ratio of 2.7).

Barucci, M.A., Fulchignoni, M., Fornasier, S., Dotto, E., Vernazza, P., Birlan, M., Binzel, R.P., Carvano, J.M., Merlin, F., Barbieri, C., Belskaya, I.N., 2005. Asteroid target selection for the new Rosetta mission baseline. 21 Lutetia and 2867 Steins. Astronomy and Astrophysics 430, 313–317.

Berthier, J., Frappa, E., Klotz, A., Lecacheux, J., Descamps, P., Vachier, F., Marchis, F., Bendjoya, P., Abe, L., Suarez, O., Tanga, P., Devogele, M., Dubreuil, P., Preston, S., 2013. Detection of a Stellar Occultation by (87) Sylvia I (Romulus). Central Bureau Electronic Telegrams 3398.

Blanco, C., di Martino, M., Gonano, M., Jaumann, R., Mottola, S., 1989. CCD observations of minor planets. Memorie della Societa Astronomica Italiana 60, 195–198.

Bottke, Jr., W.F., Richardson, D.C., Michel, P., Love, S.G., 1999. 1620 Geographos and 433 Eros: Shaped by Planetary Tides? Astronomical Journal 117, 1921–1928.

Bouchez, A.H., Brown, M.E., Campbell, R., Chin, J., van Dam, M., Hartman, S., Johansson, E., Lafon, R., Le Mignant, D., Rabinowitz, D., Sari, R., Stomski, P., Summers, D., Trujillo, C., Wizinowich, P., 2006. Keck Laser Guide Star Adaptive Optics Discovery and Characterization of Large Kuiper Belt Object Satellites, in: American Astronomical Society Meeting Abstracts #207, p. 98.09.

Brown, M.E., Bouchez, A.H., Rabinowitz, D., Sari, R., Trujillo, C.A., van Dam, M., Campbell, R., Chin, J., Hartman, S., Johansson, E., Lafon, R., Le Mignant, D., Stomski, P., Summers, D., Wizinowich, P., 2005. Keck Observatory Laser Guide Star Adaptive Optics Discovery and Characterization of a Satellite to the Large Kuiper Belt Object 2003 EL_{61}. Astrophysical Journal 632, L45–L48.

Brown, M.E., Margot, J.L., Keck, II, W.M., de Pater, I., Roe, H., 2001. S/2001 (87) 1. Central Bureau Electronic Telegrams 7588.

Brozović, M., Benner, L.A.M., Taylor, P.A., Nolan, M.C., Howell, E.S., Magri, C., Scheeres, D.J., Giorgini, J.D., Pollock, J.T., Pravec, P., Galád, A., Fang, J., Margot, J.L., Busch, M.W., Shepard, M.K., Reichart, D.E., Ivarsen, K.M., Haislip, J.B., Lacluyze, A.P., Jao, J., Slade, M.A., Lawrence, K.J., Hicks, M.D., 2011. Radar and optical observations and physical modeling of triple near-Earth Asteroid (136617) 1994 CC. Icarus 216, 241–256.

Bus, S.J., Binzel, R.P., 2002. Phase II of the Small Main-Belt Asteroid Spectroscopic Survey A Feature-Based Taxonomy. Icarus 158, 146–177.

Carry, B., 2012. Density of asteroids. Planetary and Space Science 73, 98–118.

Carry, B., Dumas, C., Kaasalainen, M., Berthier, J., Merline, W.J., Erard, S., Conrad, A., Drummond, J.D., Hestroffer, D., Fulchignoni, M., Fusco, T., 2010. Physical properties of (2) Pallas. Icarus 205, 460–472.

Carry, B., Kaasalainen, M., Merline, W.J., Müller, T.G., Jorda, L., Drummond, J.D., Berthier, J., O'Rourke, L., Ďurech, J., Küppers, M., Conrad, A., Tamblyn, P., Dumas, C., Sierks, H., Osiris Team, 2012. Shape modeling technique KOALA validated by ESA Rosetta at (21) Lutetia. Planetary & Space Science 66, 200–212.

Descamps, P., Marchis, F., Berthier, J., Emery, J.P., Duchêne, G., de Pater, I., Wong, M.H., Lim, L., Hammel, H.B., Vachier, F., Wiggins, P., Teng-Chuen-Yu, J.P., Peyrot, A., Pollock, J., Assafin, M., Vieira-Martins, R., Camargo, J.I.B., Braga-Ribas, F., Macomber, B., 2011. Triplicity and physical characteristics of Asteroid (216) Kleopatra. Icarus 211, 1022–1033.

Descamps, P., Marchis, F., Pollock, J., Berthier, J., Vachier, F., Birlan, M., Kaasalainen, M., Harris, A.W., Wong, M.H., Romanishin, W.J., Cooper, E.M., Kettner, K.A., Wiggins, P., Kryszczynska, A., Polinska, M., Coliac, J.F., Devyatkin, A., Verestchagina, I., Gorshanov, D., 2008. New determination of the size and bulk density of the binary Asteroid 22 Kalliope from observations of mutual eclipses. Icarus 196, 578–600.

Devillard, N., 1997. The eclipse software. The Messenger 87, 19–20.

Drummond, J.D., Cocke, W.J., 1989. Triaxial ellipsoid dimensions and rotational pole of 2 Pallas from two stellar occultations. Icarus 78, 323–329.

Dunham, D.W., Herald, D., Frappa, E., Hayamizu, T., Talbot, J., Timerson, B., 2012. Asteroid occultations v10.0. ear-a-3-rdr-occultations-v10.0. NASA Planetary Data System .

Eisenhauer, F., Abuter, R., Bickert, K., Biancat-Marchet, F., Bonnet, H., Brynnel, J., Conzelmann, R.D., Delabre, B., Donaldson, R., Farinato, J., Fedrigo, E., Genzel, R., Hubin, N.N., Iserlohe, C., Kasper, M.E., Kissler-Patig, M., Monnet, G.J., Roehrle, C., Schreiber, J., Stroebele, S., Tecza, M., Thatte, N.A., Weisz, H., 2003. SINFONI - Integral field spectroscopy at 50 milliarcsecond resolution with the ESO VLT, in: Iye, M., Moorwood, A.F.M. (Eds.), Society of Photo-Optical Instrumentation Engineers (SPIE) Conference Series, pp. 1548–1561.

Esposito, S., Riccardi, A., Pinna, E., Puglisi, A., Quirós-Pacheco, F., Arcidiacono, C., Xompero, M., Briguglio, R., Agapito, G., Busoni, L., Fini, L., Argomedo, J., Gherardi, A., Brusa, G., Miller, D., Guerra, J.C., Stefanini, P., Salinari, P., 2011. Large Binocular Telescope Adaptive Optics System: new achievements and perspectives in adaptive optics, in: Society of Photo-Optical Instrumentation Engineers (SPIE) Conference Series.

Fang, J., Margot, J.L., Brozovic, M., Nolan, M.C., Benner, L.A.M., Taylor, P.A., 2011. Orbits of Near-Earth Asteroid Triples 2001 SN263 and 1994 CC: Properties, Origin, and Evolution. Astrophysical Journal 141.

Fang, J., Margot, J.L., Rojo, P., 2012. Orbits, Masses, and Evolution of Main Belt Triple (87) Sylvia. AJ 144, 70.

Fornasier, S., Clark, B.E., Dotto, E., 2011. Spectroscopic survey of X-type asteroids. Icarus 214, 131–146.

Frouard, J., Compère, A., 2012. Instability zones for satellites of asteroids: The example of the (87) Sylvia system. Icarus 220, 149–161.

Ghosh, A., Weidenschilling, S.J., McSween, Jr., H.Y., 2003. Importance of the accretion process in asteroid thermal evolution: 6 Hebe as an example. Meteoritics and Planetary Science 38, 711–724.

Hanuš, J., Marchis, F., Ďurech, J., 2013a. Sizes of main-belt asteroids by combining shape models and Keck adaptive optics observations. Icarus 226, 1045–1057.

Hanuš, J., Ďurech, J., Brož, M., Marciniak, A., Warner, B.D., Pilcher, F., Stephens, R., Behrend, R., Carry, B., Čapek, D., Antonini, P., Audejean, M., Augustesen, K., Barbotin, E., Baudouin, P., Bayol, A., Bernasconi, L., Borczyk, W., Bosch, J.G., Brochard, E., Brunetto, L., Casulli, S., Cazenave, A., Charbonnel, S., Christophe, B., Colas, F., Coloma, J., Conjat, M., Cooney, W., Correira, H., Cotrez, V., Coupier, A., Crippa, R., Cristofanelli, M., Dalmas, C., Danavaro, C., Demeautis, C., Droege, T., Durkee, R., Esseiva, N., Esteban, M., Fagas, M., Farroni, G., Fauvaud, M., Fauvaud, S., Del Freo, F., Garcia, L., Geier, S., Godon, C., Grangeon, K., Hamanowa, H., Hamanowa, H., Heck, N., Hellmich, S., Higgins, D., Hirsch, R., Husarik, M., Itkonen, T., Jade, O., Kamiński, K., Kankiewicz, P., Klotz, A., Koff, R.A., Kryszczyńska, A., Kwiatkowski, T., Laffont, A., Leroy, A., Lecacheux, J., Leonie, Y., Leyrat, C., Manzini, F., Martin, A., Masi, G., Matter, D., Michałowski, J., Michałowski, M.J., Michałowski, T., Michelet, J., Michelsen, R., Morelle, E., Mottola, S., Naves, R., Nomen, J., Oey, J., Ogłoza, W., Oksanen, A., Oszkiewicz, D., Pääkkönen, P., Paiella, M., Pallares, H., Paulo, J., Pavic, M., Payet, B., Polińska, M., Polishook, D., Poncy, R., Revaz, Y., Rinner, C., Rocca, M., Roche, A., Romeuf, D., Roy, R., Saguin, H., Salom, P.A., Sanchez, S., Santacana, G., Santana-Ros, T., Sareyan, J.P., Sobkowiak, K., Sposetti, S., Starkey, D., Stoss, R., Strajnic, J., Teng, J.P., Trégon, B., Vagnozzi, A., Velichko, F.P., Waelchli, N., Wagrez, K., Wücher, H., 2013b. Asteroids' physical models from combined dense and sparse photometry and

scaling of the YORP effect by the observed obliquity distribution. Astronomy and Astrophysics 551, A67.

Harris, A.W., Young, J.W., 1980. Asteroid rotation. III - 1978 observations. Icarus 43, 20–32.

Herriot, G., Morris, S., Anthony, A., Derdall, D., Duncan, D., Dunn, J., Ebbers, A.W., Fletcher, J.M., Hardy, T., Leckie, B., Mirza, A., Morbey, C.L., Pfleger, M., Roberts, S., Shott, P., Smith, M., Saddlemyer, L.K., Sebesta, J., Szeto, K., Wooff, R., Windels, W., Veran, J.P., 2000. Progress on Altair: the Gemini North adaptive optics system, in: Wizinowich, P.L. (Ed.), Society of Photo-Optical Instrumentation Engineers (SPIE) Conference Series, pp. 115–125.

Hodapp, K.W., Jensen, J.B., Irwin, E.M., Yamada, H., Chung, R., Fletcher, K., Robertson, L., Hora, J.L., Simons, D.A., Mays, W., Nolan, R., Bec, M., Merrill, M., Fowler, A.M., 2003. The Gemini Near-Infrared Imager (NIRI). Publications of the Astronomical Society of the Pacific 115, 1388–1406.

Kaasalainen, M., 2011. Multimodal inverse problems: maximum compatibility estimate and shape reconstruction. Inverse Problems and Imaging 5, 37–37.

Kaasalainen, M., Torppa, J., Piironen, J., 2002. Models of Twenty Asteroids from Photometric Data. Icarus 159, 369–395.

Lagerkvist, C.I., Barucci, M.A., Capria, M.T., Fulchignoni, M., Guerriero, L., Perozzi, E., Zappala, V., 1987. Asteroid photometric catalogue.

Lenzen, R., Hartung, M., Brandner, W., Finger, G., Hubin, N.N., Lacombe, F., Lagrange, A.M., Lehnert, M.D., Moorwood, A.F.M., Mouillet, D., 2003. NAOS-CONICA first on sky results in a variety of observing modes, in: Iye, M., Moorwood, A.F.M. (Eds.), Society of Photo-Optical Instrumentation Engineers (SPIE) Conference Series, pp. 944–952.

Marchis, F., Baek, M., Berthier, J., Descamps, P., Hestoffer, D., Kaasalainen, M., Vachier, F., 2006a. Large Adaptive Optics Survey of Asteroids (LAOSA):

Size, Shape, and Occasionally Density via Multiplicity. LPI Contributions 1325, 57–58.

Marchis, F., Descamps, P., Hestroffer, D., Berthier, J., 2005a. Discovery of the triple asteroidal system 87 Sylvia. Nature 436, 822–824.

Marchis, F., Descamps, P., Hestroffer, D., Berthier, J., Brown, M.E., Margot, J.L., 2005b. Satellites of (87) Sylvia. Central Bureau Electronic Telegrams 8582, 1.

Marchis, F., Kaasalainen, M., Hom, E.F.Y., Berthier, J., Enriquez, J., Hestroffer, D., Le Mignant, D., de Pater, I., 2006b. Shape, size and multiplicity of main-belt asteroids. I. Keck Adaptive Optics survey. Icarus 185, 39–63.

Marchis, F., Lainey, V., Descamps, P., Berthier, J., van Dam, M., de Pater, I., Macomber, B., Baek, M., Le Mignant, D., Hammel, H.B., Showalter, M., Vachier, F., 2010. A dynamical solution of the triple asteroid system (45) Eugenia. Icarus 210, 635–643.

Marchis, F., Ruffio, J.B., Vachier, F., Berthier, J., 2013a. Component-resolved near-infrared spectra of multiple asteroid systems. AGU Fall Meeting Abstracts .

Marchis, F., Vachier, F., Ďurech, J., Enriquez, J.E., Harris, A.W., Dalba, P.A., Berthier, J., Emery, J.P., Bouy, H., Melbourne, J., Stockton, A., Fassnacht, C.D., Dupuy, T.J., Strajnic, J., 2013b. Characteristics and large bulk density of the C-type main-belt triple asteroid (93) Minerva. Icarus 224, 178–191.

Ockert-Bell, M.E., Clark, B.E., Shepard, M.K., Isaacs, R.A., Cloutis, E.A., Fornasier, S., Bus, S.J., 2010. The composition of M-type asteroids: Synthesis of spectroscopic and radar observations. Icarus 210, 674–692.

Ostro, S.J., Jurgens, R.F., Rosema, K.D., Hudson, R.S., Giorgini, J.D., Winkler, R., Yeomans, D.K., Choate, D., Rose, R., Slade, M.A., Howard, S.D., Scheeres, D.J., Mitchell, D.L., 1996. Radar Observations of Asteroid 1620 Geographos. Icarus 121, 46–66.

Pogson, N., 1866. Minor Planet 87 Sylvia. MNRAS 26, 311.

Press, W., Teukolsky, S., Vetterling, W., Flannery, B., 2007. Numerical Recipes: The Art of Scientific Computing.

Prokof'eva, V.V., Demchik, M.I., 1992. Asteroid 87 Sylvia is binary. Astronomicheskij Tsirkulyar 1552, 27–28.

Prokof'eva, V.V., Demchik, M.I., 1994. Fourier analysis of simultaneous BVR observations of the asteroid 87 Sylvia and its duplicity. Astronomy Letters 20, 245–252.

Prokof'eva, V.V., Demchik, M.L., Karachkina, L.G., 1995. Photometric Evidences for the Binary Asteroids 87 Sylvia and 423 Diotima. Astronomical and Astrophysical Transactions 8, 291–295.

Ragozzine, D., Brown, M.E., 2009. Orbits and Masses of the Satellites of the Dwarf Planet Haumea (2003 EL61). Astrophysical Journal 137, 4766–4776.

Rousset, G., Lacombe, F., Puget, P., Hubin, N.N., Gendron, E., Fusco, T., Arsenault, R., Charton, J., Feautrier, P., Gigan, P., Kern, P.Y., Lagrange, A.M., Madec, P.Y., Mouillet, D., Rabaud, D., Rabou, P., Stadler, E., Zins, G., 2003. NAOS, the first AO system of the VLT: on-sky performance, in: Wizinowich, P.L., Bonaccini, D. (Eds.), Society of Photo-Optical Instrumentation Engineers (SPIE) Conference Series, pp. 140–149.

Schober, H.J., Surdej, J., 1979. UBV photometry of the asteroids 9 Metis, 87 Sylvia and 247 Eukrate during their oppositions in 1978 with respect to lightcurves. Astronomy and Astrophysics Supplements 38, 269–274.

Storrs, A., Vilas, F., Landis, R., Wells, E., Woods, C., Zellner, B., Gaffey, M., 2001. S/2001 (87) 1. Central Bureau Electronic Telegrams 7590, 3.

Tedesco, E.F., Noah, P.V., Noah, M., Price, S.D., 2002. The Supplemental IRAS Minor Planet Survey. Astronomical Journal 123, 1056–1085.

Timerson, B., Brooks, J., Conard, S., Dunham, D.W., Herald, D., Tolea, A., Marchis, F., 2013. Occultation Evidence for a Satellite of the Trojan Asteroid (911) Agamemnon. ArXiv e-prints .

Ďurech, J., Grav, T., Jedicke, R., Denneau, L., Kaasalainen, M., 2005. Asteroid Models from the Pan-STARRS Photometry. Earth Moon and Planets 97, 179–187.

Ďurech, J., Kaasalainen, M., Herald, D., Dunham, D., Timerson, B., Hanuš, J., Frappa, E., Talbot, J., Hayamizu, T., Warner, B.D., Pilcher, F., Galád, A., 2011. Combining asteroid models derived by lightcurve inversion with asteroidal occultation silhouettes. Icarus 214, 652–670.

Vachier, F., Berthier, J., Marchis, F., 2012. Determination of binary asteroid orbits with a genetic-based algorithm. Astronomy and Astrophysics 543, A68.

van Dam, M.A., Le Mignant, D., Macintosh, B.A., 2004. Performance of the Keck Observatory Adaptive-Optics System. Applied Optics 43, 5458–5467.

Vernazza, P., Brunetto, R., Binzel, R.P., Perron, C., Fulvio, D., Strazzulla, G., Fulchignoni, M., 2009. Plausible parent bodies for enstatite chondrites and mesosiderites: Implications for Lutetia's fly-by. Icarus 202, 477–486.

Vernazza, P., Lamy, P., Groussin, O., Hiroi, T., Jorda, L., King, P.L., Izawa, M.R.M., Marchis, F., Birlan, M., Brunetto, R., 2011. Asteroid (21) Lutetia as a remnant of Earth's precursor planetesimals. Icarus 216, 650–659.

Vokrouhlický, D., Nesvorný, D., Bottke, W.F., Morbidelli, A., 2010. Collisionally Born Family About 87 Sylvia. AJ 139, 2148–2158.

Warner, B.D., Harris, A.W., Pravec, P., 2009. The asteroid lightcurve database. Icarus 202, 134–146.

Weidenschilling, S.J., Chapman, C.R., Davis, D.R., Greenberg, R., Levy, D.H., 1990. Photometric geodesy of main-belt asteroids. III - Additional lightcurves. Icarus 86, 402–447.

Weidenschilling, S.J., Chapman, C.R., Davis, D.R., Greenberg, R., Levy, D.H., Vail, S., 1987. Photometric geodesy of main-belt asteroids. I - Lightcurves of 26 large, rapid rotators. Icarus 70, 191–245.

Weiss, B.P., Elkins-Tanton, L.T., 2013. Differentiated Planetesimals and the Parent Bodies of Chondrites. Annual Review of Earth and Planetary Sciences 41, 529–560.

Winter, O.C., Boldrin, L.A.G., Vieira Neto, E., Vieira Martins, R., Giuliatti Winter, S.M., Gomes, R.S., Marchis, F., Descamps, P., 2009. On the stability of the satellites of asteroid 87 Sylvia. MNRAS 395, 218–227.

Wizinowich, P., Adkins, S., Dekany, R., Gavel, D., Max, C., Bartos, R., Bell, J., Bouchez, A., Chin, J., Conrad, A., Delacroix, A., Johansson, E., Kupke, R., Lockwood, C., Lyke, J., Marchis, F., McGrath, E., Medeiros, D., Morris, M., Morrison, D., Neyman, C., Panteleev, S., Pollard, M., Reinig, M., Stalcup, T., Thomas, S., Troy, M., Tsubota, K., Velur, V., Wallace, K., Wetherell, E., 2010. W. M. Keck Observatory's next-generation adaptive optics facility, in: Society of Photo-Optical Instrumentation Engineers (SPIE) Conference Series.

Wizinowich, P.L., Acton, D.S., Lai, O., Gathright, J., Lupton, W., Stomski, P.J., 2000. Performance of the W.M. Keck Observatory Natural Guide Star Adaptive Optic Facility: the first year at the telescope, in: Wizinowich, P.L. (Ed.), Society of Photo-Optical Instrumentation Engineers (SPIE) Conference Series, pp. 2–13.